UC San Diego
UC San Diego Electronic Theses and Dissertations

Title
Surface Preparation of Gallium Nitride for Atomic Layer Deposition of Aluminum Oxide

Permalink
https://escholarship.org/uc/item/1vr035n0

Author
Kerr, Amanda J.

Publication Date
2014

Peer reviewed|Thesis/dissertation

eScholarship.org Powered by the California Digital Library
University of California

UNIVERSITY OF CALIFORNIA, SAN DIEGO

Surface Preparation of Gallium Nitride for Atomic Layer Deposition of Aluminum Oxide

A thesis submitted in partial satisfaction of the requirements for the degree Master of Science

in

Electrical Engineering (Applied Physics)

by

Amanda J. Kerr

Committee in Charge:

Professor Andrew Kummel, Chair
Professor Peter Asbeck, Co-Chair
Professor Yuhwa Lo, Member
Professor Fainman, Member

2014

Copyright

Amanda J. Kerr, 2014

All rights reserved

The thesis of Amanda J. Kerr is approved, and it is acceptable in quality and form for publication on microfilm and electronically:

____

____

____

Co-Chair

____

Chair

University of California, San Diego

2014

TABLE OF CONTENTS

SIGNATURE PAGE iii
TABLE OF CONTENTS iv
LIST OF FIGURES vi
LIST OF TABLES vii
LIST OF SYMBOLS AND ABBREVIATIONS viii
ACKNOWLEDGEMENTS ix
ABSTRACT OF THE THESIS xi
CHAPTER ONE 1
INTRODUCTION 1
1.1 Preview *1*
1.2 Overview of ALD *3*
1.3 Chemistry of TMA and Water ALD *5*
1.4 Figures *9*
CHAPTER TWO 11
ALD PROCESS DEVELOPMENT 11
2.1 Background *11*
2.2 Experimental Setup *12*
A. Reactor Design 12
B. ALD Optimization 13
C. ALD Pretreatment 15
2.3 Results *18*
B. Pretreatment Optimization 20
2.4 Discussion *22*
2.5 Conclusions *25*
2.6 Figures *26*
CHAPTER THREE 32
PREPARATION OF GALLIUM NITRIDE SURFACES FOR ATOMIC LAYER DEPOSITION OF ALUMINUM OXIDE 32
3.1 Abstract *32*
3.2 Background *32*
3.3 Experimental Modeling and Details *34*
A. DFT-MD Modeling 34
B. Cleaning Study 35
3.4 Results and Discussion *38*

A. DFT Modeling 38
B. Cleaning Study 43
3.5 Conclusion *47*
3.6 Acknowledgements *48*
3.7 Figures *49*

REFERENCES 54

LIST OF FIGURES

Figure 1.1. Diagrams of a) a perpendicular type reactor and b) a flow type reactor. 9

Figure 1.2. A cartoon illustrating the chemistry and deposition mechanics of the TMA and water ALD process...10

Figure 2.1. Schematic of the Beneq TFS-200 ALD chamber.................................. 26

Figure 2.2. A study exploring the effects of TMA and water pulse lengths 27

Figure 2.3. A study of the effects of purge time on the resulting film quality.. 28

Figure 2.4. A study of the effects of hydrogen plasma power during the pretreatment on oxide quality 29

Figure 2.5. 5µm x 5µm AFM images of GaN surfaces treated with 5 cycles of H/TMA/H at varying plasma powers.. 30

Figure 2.6. A study examining hydrogen plasma exposure times on the film. 31

Figure 3.1. DFT simulations for a-Al2O3/ordered O-Ga-O interlayer/GaN(0001). .. 49

Figure 3.2. DFT simulations for a-Al2O3/GaN(0001) 50

Figure 3.3. *In-situ* XPS study of the effect of annealing on wet cleaned GaN(0001). 51

Figure 3.4. In_Situ XPS study of a sulfur 2s GaN(0001) and GaAs(001) treated with $(NH_4)_2S$.. 52

Figure 3.5. *Ex-situ* angle resolved XPS of a-Al_2O_3/GaN(0001) stack. 53

LIST OF TABLES

Table 2.1. Summary of ALD Experiment 1 15

Table 2.2. Summary of ALD Experiment 2 15

Table 2.3. Plasma Pretreatment Conditions for Power Study 17

Table 2.4. Plasma Pretreatment Conditions for Cycle Study 17

Table 3.1. Summary of ALD Pretreatments 37

Table 3.2. Summary of Trap Densities.. 46

LIST OF SYMBOLS AND ABBREVIATIONS

Aluminum	Al
Aluminum Oxide	Al_2O_3
Ammonium Hydroxide	NH_4OH
Ammonium Sulfide	$(NH_4)_2S$
Angstrom	Å
Argon	Ar
Atomic Force Microscopy	AFM
Atomic Layer Deposition	ALD
Capacitance-Voltage	C-V
Chemical Vapor Deposition	CVD
Dimethylaluminum	DMA
Density Functional Theory	DFT
Density of States	DOS
High Electron Mobility Transistor	HEMT
Enhancement-Mode High Electron Mobility Transistor	EHEMT
Farrad	F
Gallium	Ga
Gallium Arsenide	GaAs
Gallium Nitride	GaN
Gibbs Free Energy of Formation	ΔG
Indium Gallium Arsenide	InGaAs
Hydrochloric Acid	HCl
Hydrogen Peroxide	H_2O_2
Metal-Oxide-Semiconductor Capacitor	MOSCAP
Metal-Oxide-Semiconductor High Electron Mobility Transistor	MOS-HEMT
Metal-Oxide-Semiconductor Field Effect Transistor	MOSFET
Monolithic Microwave Integrated Circuit	MMIC
Monomethylaluminum	MMA
Nitrogen	N
Oxygen	O
Radio Frequency	RF
Trimethylaluminum	TMA
Volt	V
X-Ray Photoelectron Spectroscopy	XPS

ACKNOWLEDGEMENTS

I would like to thank my Advisor, Andrew Kummel, for the opportunity to be a member of his group. I have grown leaps and bounds in the last 18 months as a part of this group. I have had so many great experiences that I will carry with me for the rest of my carrier. I may not have loved it at the time, but thank you for encouraging me to develop my own ideas and techniques, write papers, and speak in front of the scientific community.

I would also like to thank my fellow Kummel Group lab mates for accepting a lowly master's student as one of their own. You have all become such great friends, and I will miss the time we spent together both in and outside of lab. You helped me to survive UCSD and introduced me to all the awesome things about San Diego. I had the chance to work with most of you at some point over the past two years, and nearly all the knowledge I have gained, I owe to you. I would especially like to thank Tobin Kaufman-Osborn and Kasra Sardashti. Tobin, you guided me through the foreign land of surface chemistry, comforted me when I was nervous for my first talk, and gave me advice on writing my first paper. I will always appreciate the time you took to teach me STM, XPS, and the specifics of surface interactions. You were my senior student but always treated me as an equal. Kasra, we toiled day and sometimes night together to make something work from nothing. We had a lot of fun, but also our share of frustration, which I could not have gotten through without you. I will miss all of our discussions over coffee and road trips to UCSB, but most of all, I will miss your ability to help me work out a difficult problem. I would not have been able to

complete this thesis without you. You were a great friend to me and we made a pretty amazing team. I know we will continue to be friends long after grad school.

I could not have completed this degree without the support of my friends and family. I would like to thank my parents for encouraging me to pursue this degree. I would especially like to thank my mother for all of her kindness, love, and mostly for the endless supply of cookies. Those cookies fueled many a late night of writing. I would also like to thank my husband, Steve, who showed me unwavering love and support throughout this experience. He sacrificed more in the past 2 years for my dreams than I can list here.

Lastly, and most importantly, I would like to thank my friends and coworkers at Raytheon for believing in me. Without the financial support of the Advanced Studies Program, my experience at UCSD and with the Kummel Group would not have been possible. I look forward to returning home and sharing everything I have learned with all of you!

The work in this thesis was funded by the SRC, MARCO, DARPA, and the ONR. A portion of this work was performed at the California Institute for Telecommunications and Information Technology Nano3 facility, and I would like to thank the staff for all of their hard work in helping me develop what is presented here.

At the time of this writing, Chapter 3 is a reprint of work which has been submitted for publication.

A.J. Kerr, E. Chagarov, S. Gu, T. Kaufman-Osborn, S. Madisetti, J. Wu, P.M. Asbeck, S. Oktyabrsky, A.C. Kummel "Preparation of Gallium Nitride Surfaces for Atomic Layer Deposition of Aluminum Oxide"

ABSTRACT OF THE THESIS

Surface Preparation of Gallium Nitride for Atomic Layer Deposition of Aluminum Oxide

by

Amanda J. Kerr

Master of Science in Electrical Engineering (Applied Physics)

University of California, San Diego, 2014

Professor Andrew Kummel, Chair

Professor Peter Asbeck, Co-Chair

Surface cleaning of gallium nitride (GaN) prior to atomic layer deposition (ALD) of aluminum oxide was investigated at both the atomic as well as device level. Two studies were performed, one in which an ALD process was developed and a

second which explored the atomic level origins of defects in the Al_2O_3/GaN system. An ALD process was developed such that a high quality aluminum oxide gate dielectric could be deposited on GaN with only the use of an in-situ TMA pretreatment. This process was developed using a flow type reactor which allowed for the elimination of a hydrogen plasma surface treatment.

In the second study, density functional theory modeling was used to examine the likely sources of defects in the Al_2O_3Al2O3/GaN(0001) system. The modeling revealed that Al_2O_3 is able to passivate the majority of defect states on the GaN(0001) surface, but nucleation of oxide in every unit cell would be required to completely eliminate them. The use of a two-step surface treatment involving a wet clean in HCl and NH_4OH to remove native oxide followed by an in-situ dry clean using hydrogen and TMA was shown to improve the nucleation density. Calculated Dit values were reduced by a factor of 2-3 while border trap densities were reduced a full order of magnitude.

CHAPTER ONE

Introduction

1.1 Preview

The trend in both the RF and power device industries has been to continually push the extremes of electronics in terms of RF power output, speed, and breakdown fields. This push has led these industries to expand beyond the realm of mainstream silicon technologies and adopt new materials and device architectures. One material system that has received an increasing amount of attention over the last decade is gallium nitride (GaN). The wide band gap semiconductor offers high electron mobility, high saturation velocity, and high breakdown voltage, all of which make it an attractive candidate for RF and power electronics.

The RF and power industries have both adopted GaN, but the applications have a wide range of device requirements. One of the most common device architectures is a high electron mobility transistor (HEMT) utilizing AlGaN/GaN or InAlN/GaN quantum wells. These devices have the advantage of large electron mobilities due to the quantum well confinement as well as high breakdown voltages[1-4]. However, the issue with GaN HEMTs is that they are normally-on (depletion mode) devices. For some applications, this results in unacceptable levels of standby power consumption as well as adds extra complexity to circuits due to the need for additional power supplies. Additionally, the band offset between AlGaN or InAlN and GaN is typically small which makes HEMTs susceptible to gate leakage. Reliability issues are one of the key obstacles preventing widespread adoption of this technology[5].

There are other device architectures, however, that have been developed to create normally-off (enhancement mode) transistors. The most common of these is the metal-oxide-semiconductor field effect transistor (MOSFET). These devices have the advantage of being normally-off as well as having a large band offset which make them less susceptible to leakage. The drawback, though, is that they do not exhibit the high electron mobilities realized in HEMT structures. Both HEMTs and MOSFETs are viable structures, but there has also been research into combining both technologies to create a hybrid MOS-HEMT[6-9] or enhancement mode HEMT (EHEMT)[10-12].

One common feature shared by MOSFETs and MOSHEMTs is that they utilize insulated gates. While there are advantages to using insulated gate structures, such as reduced gate leakage and standby power consumption, there are several challenges still impeding their widespread adoption. One of the most critical of these is the creation of low-defect interfaces between the gate dielectrics and underlying GaN. Failure to form a low-defect oxide/GaN interface can severely impact the device performance in that defects cause degradation of carrier mobility, time-dependent breakdown, anomalous current outputs, as well as Fermi level pinning[13].

The work presented in this thesis is focused upon understanding the atomic interactions occurring at gate oxide/GaN interfaces and optimizing dielectric deposition processes that minimize the formation of interfacial and bulk oxide defects.

1.2 Overview of ALD

There are many existing options for depositing gate dielectrics, but one method in particular has become the favored approach for this task. Atomic layer deposition (ALD) is a modified chemical vapor deposition technique that uses gaseous precursors which react on a substrate surface to form the desired gate dielectric. What differentiates ALD from other vapor deposition processes is that precursor materials are introduced to the reactor in separate stages. Each precursor is allowed to fully saturate the substrate surface before the next precursor is introduced. Because surface coverage is limited to a maximum of one monolayer, growth is subsequently self-limiting. The self-limiting nature of ALD growth allows for extremely precise control over film thickness down to the angstrom range. Additionally, because single precursors are able to adsorb onto every area of a substrate before reacting, the resulting film is highly conformal to features on the surface.

In general, there are two key factors to consider when designing an ALD process—the first being precursor chemistry. Precursors for use in ALD should satisfy a few critical requirements. The first requirement is to be volatile, or able to be volatilized at elevated temperature, since ALD is a vapor phase technique. They must also be resistant to decomposition as this can result in unintentional CVD growth. Secondly, any precursors must be highly reactive with each other (the desired reaction product should have a very negative ΔG of formation)[14]. This ensures that the surface reactions will proceed quickly to completion. Along these same lines, the precursors and their byproducts should cause minimum etching of the substrate or underlying films. Byproducts should also be volatile so that they may be easily purged from the

chamber, thereby preventing any contamination of the film as growth proceeds. Satisfying all of these criteria simultaneously can be very difficult and has greatly limited the number of precursors available for ALD processes. Precursor innovation is still an active area of research both academically and commercially[15-19]. For ALD deposition of gate oxides, there are generally two categories of precursors needed. The first precursor supplies the metal atom and is typically an organometallic or metal halide compound[20]. The second precursor is the non-metal oxidant, by far the most common of which are hydrides such as H_2O, H_2O_2, or NH_3[14, 21]. Recently, though, plasmas of O_2, N_2, and NH_3[14, 21] have been successfully used as sources for the nonmetal half-cycle.

The second key factor in ALD is the design of the reactor system. There are many types of reactors available, but the two most common are flow and perpendicular[14]. Figure 1.1 shows two examples of these types of systems. In a flow type reactor, an inert carrier gas is constantly streamed over the sample surface at high pressure (i.e more than 0.1 torr). Precursor gases are pulsed into this stream and carried laterally across the sample. The reactions proceed as the precursors absorb to the substrate. In this manner, the side of the substrate nearest to the gas inlet line is exposed to the precursors first. In flow type systems, there is never a point during the deposition where the carrier gas flow is ceased, so the pressure remains relatively high (1-5 Torr)[22]. In perpendicular type systems, an inert carrier gas is also used to distribute precursors; however, in this design the gases are directed from above the substrate surface. The entire substrate is exposed to precursor simultaneously. During precursor pulsing and purging, the pressure is typically kept in the range of several

hundred mTorr. Because the carrier gas disperses once it enters the reactor, processes in perpendicular type reactors may require an additional step where the carrier gas flow is ceased and the chamber is evacuated using high speed vacuum pumps. Evacuating the chamber improves the removal of excess precursor, aiding in the purge. During the pumping stages, pressures as low as $1x10^{-6}$ Torr can be achieved.

The reactor design is critical in developing a particular oxide deposition process due to the challenges each of reactors may present concerning the layout of the precursor lines, the reactor volume, substrate position relative to precursor inlets, as well as many other aspects of chamber configuration when developing a particular process. As a result, process parameters such as precursor pulse lengths, purge times, temperature, and gas flows must be tailored to accommodate particular reactor specifications.

1.3 Chemistry of TMA and Water ALD

The chemistry of each ALD process is unique in that reaction mechanisms vary amongst precursors and depend strongly on substrate surface conditions. The work in this thesis is focused upon depositing Al_2O_3 using the metalorganic compound trimethylaluminum (TMA) and water, so that process will be outlined here (see Figure 1.2). The overall reaction between TMA and water can be described by Eq. 1. This reaction describes the production of stoichiometric Al_2O_3 from TMA and water.

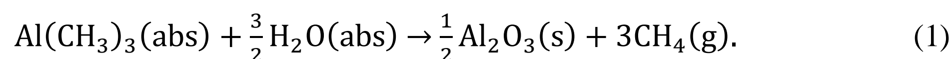

$$\mathrm{Al(CH_3)_3(abs)} + \frac{3}{2}\mathrm{H_2O(abs)} \rightarrow \frac{1}{2}\mathrm{Al_2O_3(s)} + 3\mathrm{CH_4(g)}. \quad (1)$$

In ALD, this reaction is broken into two half-reactions. The first half-cycle in which TMA is pulsed into the chamber can be described as[23]:

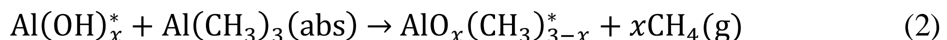

$$Al(OH)_x^* + Al(CH_3)_3(abs) \rightarrow AlO_x(CH_3)_{3-x}^* + xCH_4(g) \quad (2)$$

This equation assumes that the surface is already terminated by Al-OH bonds. The asterisk denotes the chemisorbed surface species. To begin deposition, TMA must chemisorb onto the substrate surface[14, 20, 21]. The TMA reacts after weakly absorbing to the surface so it is denoted at $Al(CH_3)_3(abs)$. As illustrated in Figure 1.2 panes 1 and 2, chemisorption of TMA occurs on active surface sites such as surface hydroxyl groups or defects[20, 21, 24-26]. Controlling the density of nucleation sites is a critical aspect of achieving defect-free films and can be affected through wet cleaning and other surface preparation methods, some of which are detailed in chapters 2 and 3[24, 27]. During the nucleation process, TMA undergoes dissociative chemisorption into dimethylaluminum (DMA) and a methyl ligand[20, 21, 24, 27, 28]. The dissociation occurs through the formation of an intermediate state in which the empty p-orbital on the Al in TMA interacts with the lone electron pairs present on the O atom in the surface hydroxyl group[29]. A methane molecule is subsequently formed and released. Also, the interaction is not limited to a single ligand. If neighboring hydroxyl sites are available, a single TMA molecule may undergo a ligand exchange reaction after initially adsorbing and form multiple bonds[29].

To truly produce self-limiting growth, the TMA dose provided must be sufficient to fully saturate the surface. This occurs either when all active sites have been exhausted or the steric interference of the methyl ligands prevents any further adsorption. At this point the surface should be methyl terminated, as shown in Figure 1.2, part 2. Once the TMA reaction has proceeded to completion, the first half-reaction in the TMA/water process is concluded by an inert gas purge. This ensures that any unreacted TMA as well as byproducts are completely expelled from the chamber.

After the purge, the second half-reaction begins. The second half-reaction corresponds to the water pulse and follows[23]:

$$\mathrm{AlO}_x(\mathrm{CH}_3)^*_{3-x} + (3-x)\mathrm{H}_2\mathrm{O(abs)} \rightarrow \mathrm{AlO}_x\mathrm{Al(OH)}^*_{3-x} + (3-x)\mathrm{CH}_4 \qquad (3)$$

During the water pulse, water molecules are introduced into the system where they dissociate on the methyl terminated surface[29]. They dissociate through the formation of the same intermediate species that forms during the TMA half-cycle[29]. The difference is the surface species is Al-CH_3 (due to methyl termination from TMA pulse) as opposed to Al-OH. Like the metal precursor dose, the water dose must also be sufficient to fully saturate the surface with hydroxyl groups. This saturation dose subsequently leaves the surface hydroxyl terminated. Another inert gas purge is performed to remove any excess water and gaseous byproducts. One issue to note is that stoichiometric oxide will be produced from the reactions described in Eq.2 and Eq.3 only when $x = 1.5$, where x corresponds to the number of methyl ligands released

during the TMA pulse. When $x < 1.5$ or $x > 1.5$, another reversible reaction will occur, see Eq.4[23], that results in recombinative desorption of water from the surface or the adsorption of a hydroxyl onto an exposed Al atom.

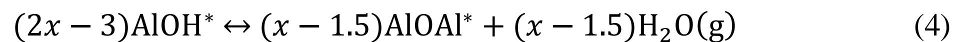

$$(2x - 3)\text{AlOH}^* \leftrightarrow (x - 1.5)\text{AlOAl}^* + (x - 1.5)\text{H}_2\text{O(g)} \quad (4)$$

The combination of the two-half reactions effectively results in alternating surface terminations, which can accumulate until the desired film thickness is achieved.

1.4 Figures

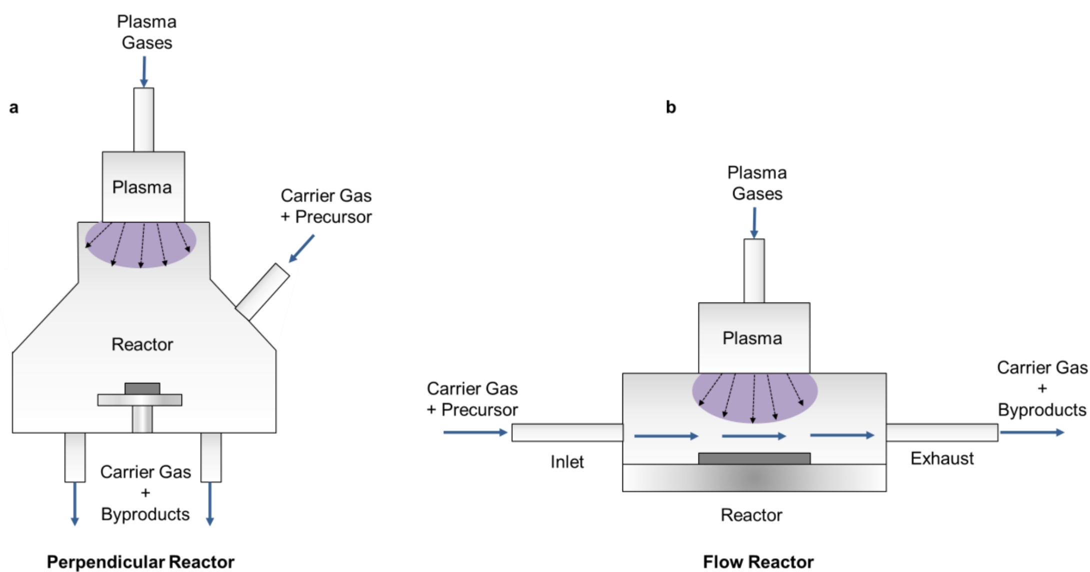

Figure 1.1. Diagrams of a) a perpendicular type reactor and b) a flow type reactor. In perpendicular type reactors, precursors enter the chamber from above and impinge on the surface uniformly. Conversely, in flow type reactors, the precursors react across the surface as they move along the stream of carrier gas.

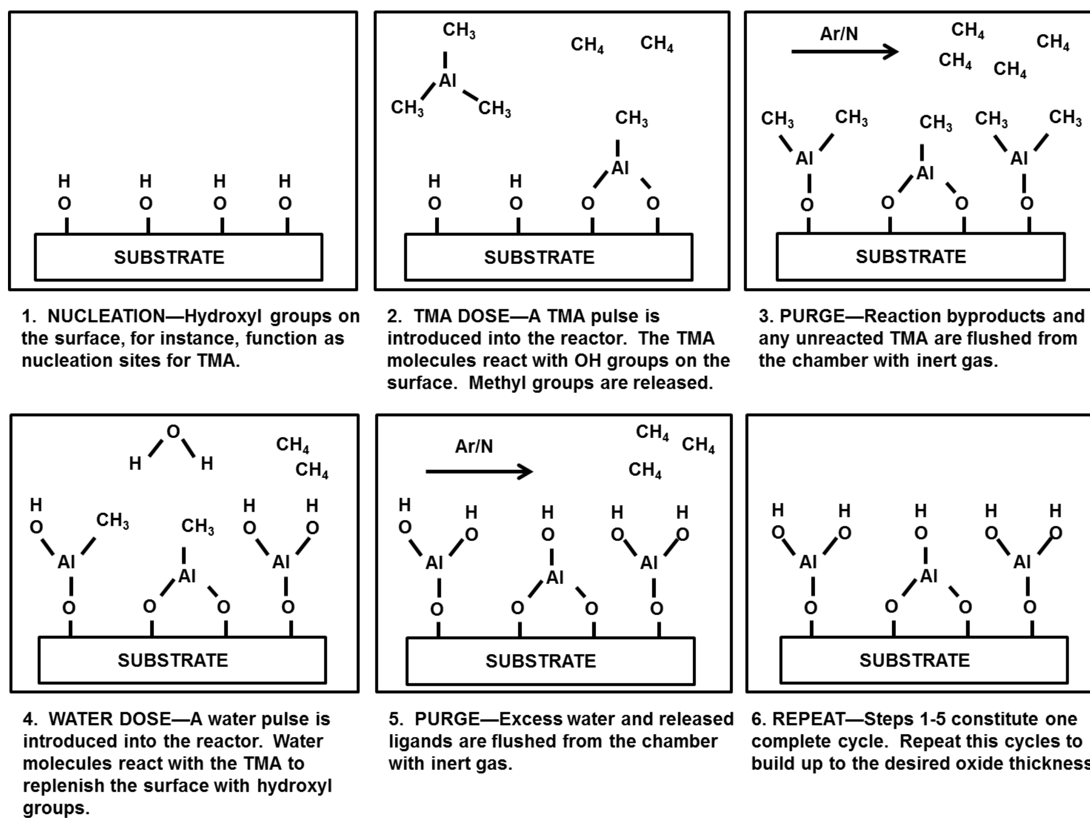

Figure 1.2. A cartoon illustrating the chemistry and deposition mechanics of the TMA and water ALD process. Steps 1-3 demonstrate TMA nucleation on the surface, TMA saturation, and puring. Steps 4-6 illustrate the water saturation dose, purge, and the final surface that has been re-hydroxylated.

CHAPTER TWO

ALD Process Development

2.1 Background

A growing movement in GaN technology is the incorporation of insulated gate devices alongside the more commonplace heterojunction transistors. This includes both MOSFETs[30] as well as MOSHEMTs[6, 7, 31]. One key area for improvement in these devices is the reduction of traps originating at the gate dielectric/GaN interface. Improving insulated gate device performance by improving the quality of the gate oxide begins by designing and optimizing a deposition process. In this case, Al_2O_3 was chosen as the gate oxide as it has a large conduction band offset with respect to GaN, has a high dielectric constant, and the necessary ALD precursors are readily available.

To ensure that interfacial and oxide traps are eliminated, the ALD must be properly nucleated and grown under optimized conditions. These traps originate at the interface between the oxide and semiconductor; therefore, the critical growth occurs within the first few cycles and will ultimately determine the quality of the final device. For this reason, controlling the state of the interface prior to growth is crucial for realizing low trap densities. Controlling the state of the semiconductor surface often involves multi-step cleaning procedures involving both wet and dry methods. Studies have demonstrated success in removing the native oxide on GaN using wet chemical solutions[32-35]. Wet cleaning is an *ex-situ* procedure; however, the substrate will inevitably be exposed to air during the loading process. To remedy this, several

groups have added *in-situ* cleaning involving TMA or plasma pulsing (with atomic H or N) immediately preceding ALD growth. Success in reducing interfacial traps has been demonstrated on InGaAs and GaAs by cycling hydrogen plasma and TMA pulses *in-situ* prior to oxide deposition[28, 29].

In an effort to replicate the improvements seen in these studies, an Al_2O_3 ALD process as well as a hydrogen plasma pretreatment combined with in ex-situ wet clean and capping was developed as part of this work. The films grown in each experiment were characterized using capacitance-voltage (CV) profiling as well as atomic force microscopy (AFM). It is noted two different ALD tools were employed. In the study described below a conventional high pressure (>0.1 torr) ALD tool with a proximal plasma was employed while the study in the following chapter a UHV ALD tool was employed because it contained a remote plasma.

2.2 Experimental Setup

A. Reactor Design

Both the *in-situ* surface pretreatment and Al_2O_3 ALD processes were designed using a Beneq TFS-200 ALD system. A diagram of the reactor setup is shown in Figure 2.1. During the deposition, a continuous stream of argon carrier gas is passed over the sample at all times. Precursor gases are pulsed into the continuous stream of carrier gas where they react on the substrate as the stream passes over the surface. Therefore, film growth proceeds as a front moving across the wafer.

For the hydrogen plasma clean, a plasma head was installed on the ceiling of the reactor directly above the sample plate. Argon purge gas was flowed through the plasma head at all times, not only to ensure even delivery of hydrogen gas but to prevent gas-phase reactions between TMA and H_2O from occurring in that space. Unlike with precursor gases, the entire sample surface receives uniform exposure to the plasma during the hydrogen pulses. During both processes, the reactor pressure was maintained at 2-2.5 mbar.

B. ALD Optimization

For the work in this thesis, Al_2O_3 films were deposited on GaN(0001) substrates grown via MOCVD. To assess the quality of these films, MOSCAP devices were fabricated and tested using C-V profiling (Agilent B1500 Semiconductor Analyzer). The MOSCAP devices consisted of approximately 8nm of Al_2O_3 deposited on GaN according to methods detailed in later sections. Palladium gates were subsequently deposited via e-beam evaporation. The GaN was grown on sapphire substrates, which are semi-insulating, thereby necessitating that contact to the GaN be made on the front side. Contacts were patterned, and the Al_2O_3 in those regions was removed by etching in a 1:10 HF solution. Palladium contacts were subsequently deposited, again using e-beam evaporation.

In total, two sets of experiments were performed to characterize the ALD process in the Beneq flow type reactor. The first experiment examined precursor dosing parameters while the second focused on purge times. Each sample first received a wet clean immediately prior to loading into the ALD chamber. This clean

consisted of a sequential dips in acetone, methanol, isopropanol, and deionized water for 1 minute each. Samples were then dipped in 7%HCl for 1 minute, 6%NH4OH for 1 minute, and deionized water for 1 minute. While the dosing and purge times were varied for each experiment, the carrier gas flows and precursor types remained constant during each deposition. Argon was used as the carrier and purge gas in both the primary process flow as well as through the plasma head. It was streamed across the sample at 200sccm and through the plasma source at 140sccm. Al_2O_3 was deposited using TMA as the metal precursor and H_2O as the oxidant. The reactor pressure ranged from 2-2.5 mbar during all depositions. All other conditions, including precursor pulse lengths, purge times, and temperature, were determined as part of the study.

The first experiment explored the effects of precursor pulse lengths on oxide and interfacial quality. This set included five samples numbered 1-5. All processing was done at 275°C. Each sample received a treatment of 5 cycles of TMA at 45ms with a 850ms purge, immediately followed by 80 cycles of ALD. The purge times for each ALD half-cycle were kept constant at 6 seconds while the TMA and H_2O pulse lengths were varied. Sample 1 had a TMA pulse time of 50ms with an H_2O pulse time of 50ms. Sample 2 had a TMA pulse time of 200ms with an H_2O pulse length of 50ms. Sample 3 had a TMA pulse time of 500ms with an H_2O pulse length of 50ms. Sample 4 had a TMA pulse time of 200ms with an H_2O pulse of 200ms. Finally, Sample 5 had a TMA pulse of 200ms with a H_2O pulse of 500ms. A summary of the parameters for each deposition is outlined in Table 2.1.

Table 2.1. Summary of ALD Experiment 1

Sample	TMA pulse length (ms)	TMA purge (s)	H_2O Pulse Length (ms)	H_2O Purge (s)
1	50	6	50	6
2	200	6	50	6
3	500	6	50	6
4	200	6	200	6
5	200	6	500	6

Note: These values reflect only the ALD conditions. Pretreatment conditions are not listed.

The second experiment involved an exploration of reactor purge times. In this case, samples were again dosed with 5 cycles of a TMA pretreatment (45ms pulse/850ms purge) followed by 80 cycles of ALD at 275°C. Precursor pulse lengths during ALD were held constant at 200ms for TMA and 50ms for H_2O for each of the three samples in this set. This time, purge times were varied at 1, 6 and 12 seconds for Samples 6, 7, and 8, respectively. Below is a summary of process conditions for this experiment in Table 2.2.

Table 2.2. Summary of ALD Experiment 2

Sample	TMA pulse length (ms)	TMA purge (s)	H_2O Pulse Length (ms)	H_2O Purge (s)
6	200	0.5	50	0.5
7	200	2	50	2
8	200	6	50	6
9	200	12	50	12

Note: These values reflect only the ALD conditions. Pretreatment conditions are not listed.

C. ALD Pretreatment

To further improve the ALD process, an *in-situ* TMA and plasma clean was developed. A series of experiments were performed to determine the optimal conditions for this treatment. The first experiment was designed to identify the plasma power that produces an improvement in interfacial quality without damaging the surface. Following the same procedure that was used in the ALD optimization experiments, all samples were first degreased in acetone, methanol isopropanol, and deionized water for 1 minute in each solution. The native oxide was then removed by dipping in 7%HCl, 6%NH_4OH, and deionized water for 1 minute in each solution. Samples were immediately loaded into the ALD chamber following this wet clean.

The ALD process for samples in this set involved two parts—an *in-situ* pretreatment and 80 cycles of Al_2O_3 deposition. The pretreatment consisted of 5 cycles of three alternating pulses of H/TMA/H following the procedure detailed by the Stemmer group[36, 37]. Each hydrogen plasma pulse was 5 seconds in length followed by a 10 second purge where the plasma power was shut off and argon was allowed to flow freely through the head. Plasma powers during these pulses were assigned as listed in Table 2.3 below. The TMA pulses included in the pretreatment were 45ms in length followed by a 850ms purge. For the 80 cycles of ALD, the TMA pulse time was 200ms, the H_2O pulse time 50ms, and the purge time 6 seconds for both the TMA and H_2O half-cycles. The entire process of in-situ pretreatment and ALD was performed at 275°C.

Table 2.3. Plasma Pretreatment Conditions for Power Study

Sample	Number of Cycles	Plasma Forward Power (W)	Plasma Pulse Length (s)
10	5	0	5
11	5	25	5
12	5	50	5
13	5	75	5
14	5	100	5
15	5	150	5

For the final set of experiments in optimizing the ALD pretreatment studied the effects of varying the number of pretreatment cycles via increasing the exposure to TMA and hydrogen. The samples in this set were first cleaned using the wet clean described in the previous sections. They were then loaded into the ALD chamber where they underwent the two-part deposition process. In this case, the number of pretreatment cycles was varied at 2, 5, and 10 cycles for samples 16, 17, and 18 respectively. The other parameters were held constant using 5 second pulses at a power of 50W. The TMA pulse length during the pretreatment was 45ms and was followed by a 850ms purge. The pretreatment was immediately followed by 80 cycles of Al_2O_3 deposition using the same conditions described for the previous set of experiments. Both the *in-situ* pretreatment and ALD growth were performed at 275°C.

Table 2.4. Plasma Pretreatment Conditions for Cycle Study

Sample	Number of Cycles	Plasma Forward Power (W)	Plasma Pulse Length (s)
15	5	75	5
16	10	75	5
17	20	75	5

2.3 Results

In the first set of experiments, the TMA and water pulse lengths were varied to determine which conditions yielded the film with the lowest leakage and densities of interface and near-interface traps. The C-V profiles for samples 1-5 are shown in Figure 2.2. The C-V plots clearly indicate that pulse lengths of 50ms TMA and 50ms H_2O (Fig.2.2a) are not sufficient to fully saturate the surface. The resulting film shows a high degree of gate leakage as evidenced by the sharp increase in capacitance and frequency dispersion beyond 1.25V. As the water pulse is increased beyond 50ms, however, there does not seem to be a significant improvement. The C-V profiles for samples with 200 and 500ms water pulses are quite similar while the films tend to improve as the TMA dose is increased. Sample 2, which had its film grown using 200ms TMA pulses and 50ms water pulses, shows greatly improved oxide quality. It exhibits a steep transition from accumulation to depletion as well as a low level of frequency dispersion in all regions. The low levels of dispersion in both accumulation and depletion are consistent with low levels of near-interface oxide traps as well as a low density of interfacial traps, respectively[38, 39]. Samples 3-5, which were grown using larger TMA and water doses, do not offer significant improvements beyond what was shown in sample 2. As a result, the conditions used in sample 2 were adopted as the base recipe for the subsequent sets of experiments.

Building on the results from the precursor pulse experiments, the purge times were examined using the optimized conditions of TMA pulse lengths of 200ms and water pulse lengths of 50ms. The multi-frequency C-V profiles for these experiments

(Samples 6-9) are shown in Figure 2.3. Sample 6 (shown in Fig.2.3a) stands out in particular as it has a significantly lower C_{ox} value as well as displays a large negative threshold voltage shift relative to samples 7-9. Both of these observations point to a CVD growth component. This film was deposited using only 500ms for purge times, which is not long enough to completely clear all unreacted precursor from the chamber following each pulse. This likely resulted in gas-phase reactions between precursor molecules and unintentional CVD oxide growth. CVD growth is not self-limiting and can deposit films with lower densities and increased defects. Additionally, the short purge times may not have completely removed reaction byproducts which could then become trapped within the oxide. All of these issues could contribute to the observed shift in threshold voltage for this sample.

The C-V profiles for samples 7-9 (Fig.2.3b-d) exhibited sharp transitions from accumulation to depletion and have similar values of C_{ox}. In this respect, all three runs produced oxide of reasonably good quality. Samples 7 and 9 both show dispersion due, at least in part, to series resistance. In this case, the resistance[40] most likely stems from non-ideal topside contacts. Published studies from other groups that also claim dispersion in accumulation can be the result of near interface traps, such as border traps, within the oxide[36, 37]. In this case, the dispersion may be due to a combination of the two. A purge length of 6 seconds was selected to ensure a robust purge for future experiments.

Overall, the series of experiments presented here allowed for identification of the optimal ALD parameters for the flow type Beneq TFS-200 reactor. For subsequent experiments, the ALD was performed at 275°C using a TMA pulse time of

200ms, a water pulse time of 50ms, and a purge time of 6 seconds following each precursor pulse.

B. Pretreatment Optimization

The second portion of the study added an *in-situ* alternating hydrogen plasma and TMA surface pretreatment to the process developed in the previous section. This particular clean was chosen as there is a long history of experimental evidence indicating that TMA, and other metalorganic molecules, are able to remove excess oxygen. This "cleanup effect" is well known on both silicon and III-V surfaces[41-47]. Additionally, atomic hydrogen provides a reducing atmosphere as well as volatilizes any carbon species on the surface. Proper surface preparation is critical as any surface unit cell in which ALD growth does not nucleate becomes a source of non-ideal bonding and the film must be grown thicker to compensate. DFT modeling detailed in Chapter 3 has shown that proper oxide nucleation can reduce the types of defects likely to form in the Al_2O_3/GaN system.

To determine the optimal conditions for the hydrogen plasma clean, the first parameter that was examined was the plasma power. This is a critical parameter as the forward power controls the strength of the plasma clean, and if the power is too high the plasma may damage the GaN surface. Figure 2.4 shows C-V profiles for pretreatments where the plasma power was varied from 0-150W. One can clearly see that the samples which have pretreatments using 25W and 50W forward power have reasonable C-V profiles. There is little dispersion in both the accumulation and threshold regions and there is a sharp transition from accumulation to depletion.

However, as the forward power is increased beyond this point, the dispersion is worsened considerably, and the maximum capacitance is reduced. An interesting point to note is that all of these samples, including those with 25W and 50W pretreatments, have poorer threshold dispersion than the samples which received only a TMA pretreatment. The hydrogen plasma instead seems to be inducing interfacial trap states, which are responsible for the visible frequency dispersion in this region.

To ascertain whether or not the surface had been damaged by the plasma, AFM images were taken for samples which received no plasma, 25W, 50W, 75W, and 100W pretreatments. No oxide was deposited on these surfaces. These AFM images can be seen in Figure 2.5. The AFM images show no discernable evidence of plasma damage at any power. This implies that the degradation in oxide quality is not due to hydrogen etching or argon ion damage, but instead stems from another aspect of the plasma system.

To ensure that the issue could not be remedied by increasing or decreasing the length of plasma exposure, films were grown in which the number of pretreatment cycles was varied at 2, 5, and 10 cycles with a control receiving only 5 cycles of TMA dosing. The results showed that the quality of the oxide was severely degraded for the sample which received 2 cycles of H/TMA/H (Fig 2.6b). The degradation of the sample shown in Fig 2.6b is likely the result of reduced TMA exposure since the number of pretreatment cycles was reduced, and those cycles also include a short TMA pulse. Those samples which received 5 and 10 cycles (Fig. 2.6c and d) showed better quality. The 5 cycles sample showed the least amount of dispersion in both accumulation and threshold, while the sample with 10 cycles yielded the highest C_{ox}.

However, the most important point to note is that the sample which received no plasma exposure is the one which has the highest C_{ox} and lowest dispersion in every region.

2.4 Discussion

Overall, these studies have shown that the plasma pretreatment did not provide a significant improvement in film or interface quality over samples which had pretreatments consisting of only 5 cycles of TMA pulses. The inclusion of the hydrogen plasma only served to introduce defects. The films grown in the Beneq TFS-200 using the *in-situ* clean of 5 cycles of TMA followed by ALD with 200ms TMA pulses, 50ms water pulses, and 6 second purges produced C-V profiles showing superior oxide quality than that of similar samples from the studies that suggested the use of the hydrogen clean. The results for the process developed in this work are very similar to those published for films that had been grown using the *in-situ* hydrogen plasma method. It is noted that the plasma in the Beneq tool is very close to the sample and may introduce radiation damage not present when employing a truly remote plasma like that in the UHV Oxford tool in the experiments described in the next chapter.

In this study, no significant differences were observed between TMA treated samples and those which received the H/TMA/H treatment, a marked decrease in film quality was observed when the TMA treatment was truncated. This indicates that the TMA clean plays a crucial role in the early stages of growth. There are several studies

that report the removal of native oxide by TMA, but that effect alone cannot explain the growth of quality films without the use of hydrogen cleaning.

The reason for this unexpected result lies in the chemistry of the pretreatment. The goal of hydrogen cleaning is to volatilize carbon species on the surface. For a surface Ga atom with carbon adsorbed onto it, the hydrogen clean may proceed as follows:

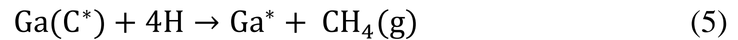

$$Ga(C^*) + 4H \rightarrow Ga^* + CH_4(g) \qquad (5)$$

This reaction involves the removal of surface carbon through the formation of methane.

However, there is another set of reactions which can occur in the presence of atomic hydrogen. The first of which involves the etching of the GaN surface through the selective removal of nitrogen in the form of ammonia.

$$N^* + 3H \rightarrow NH_3(g) \qquad (6)$$

To prevent roughening of the surface, the etch reaction must be carefully controlled. This can be done either by limiting the hydrogen dose or using an etch-stop to terminate the reaction. In this case, the TMA used in the pretreatment functioned as an etch-stop . It is hypothesized that the surface atoms with chemisorbed TMA are no longer reactive with hydrogen, and the methyl ligands effectively shield the substrate as coverage increases towards saturation. In this way,

the TMA may play a dual role. It removes residual native oxide from the surface prior to ALD and also prevents etching of the substrate.

The one caveat in utilizing TMA as a surface clean is that it is highly susceptible to oxidation. Once it is oxidized, none of the aforementioned benefits can be realized. Therefore, it is of critical importance that no residual oxidant, either from trace contaminants in the carrier gas or molecules trapped on the walls of the reactor, be allowed to reach the substrate surface. The design of the reactor becomes critical at this point. Consider a perpendicular type reactor that incorporates vacuum evacuation steps to aid in the purging process. During those steps, the pressure may be as low as the 10^{-6} Torr range. For example, at 275°C and a pressure of 1×10^{-6} Torr the mean free path of water is 293m. During the evacuation step, background water and contaminants trapped on the walls of the reactor reach the substrate and oxidize the TMA. To prevent this from occurring, the substrate must be kept in a reducing atmosphere, which the hydrogen plasma provides. In this fashion, the hydrogen plasma may also play a dual role. It volatilizes carbon species but also facilitates the TMA cleanup effect by preventing oxidation.

In contrast to the previous example, the reactor pressure in the Beneq TFS-200 system used in this study is maintained at approximately 2 mbar (1.5 Torr) for the entirety of the deposition. At this pressure and at 275°C, the mean free path of water is 195μm. This distance is considerably shorter than the distance from the reactor walls to the sample. The short mean free path combined with the carrier gas cross flow prevent water adsorbed on the reactor walls from reaching the substrate surface during the clean. As a result, the TMA can effectively remove the native oxide

without the need for a reducing atmosphere. Therefore, the hydrogen plasma can be eliminated with minimal loss of efficacy of the clean. Omission of the hydrogen clean presents a tradeoff that must be mentioned. Without the hydrogen plasma there will be no volatilization of the surface carbon, so there will consequently be a reduction in the number of active nucleation sites. However, the risk of selective nitrogen depletion is eliminated as well.

2.5 Conclusions

In conclusion, the optimization of a TMA and H_2O gate oxide process on GaN has shown that in flow type reactors such as the Beneq TFS-200 popular plasma cleaning methods may not be necessary to achieve high quality films. The films produced using the process detailed in this work have yielded results that match the film quality of published results but without the use of the hydrogen plasma.

2.6 Figures

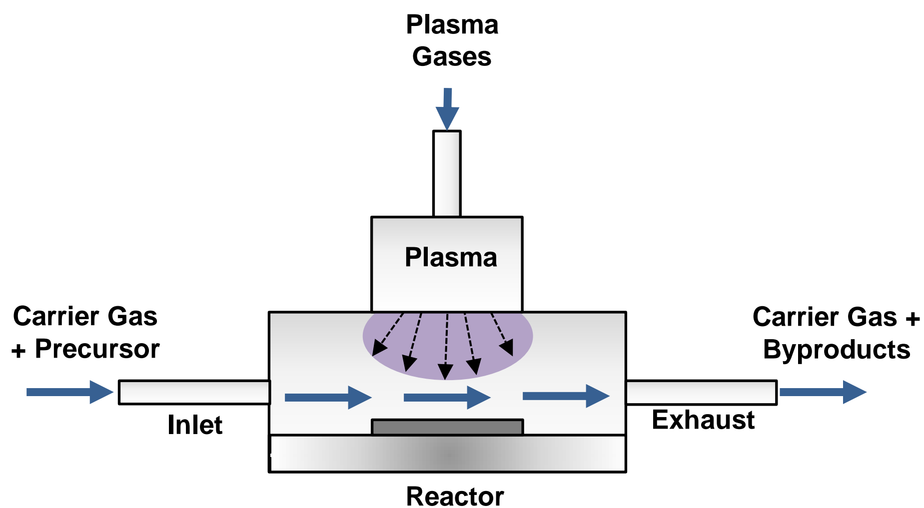

Figure 2.1. Schematic of the Beneq TFS-200 ALD chamber. A constant stream of carrier gas flows across the sample at all times. Precursor gases are pulsed into this stream where they react on the substrate from right to left. A plasma source is attached from the top of the chamber to allow for plasma cleaning or plasma enhanced ALD.

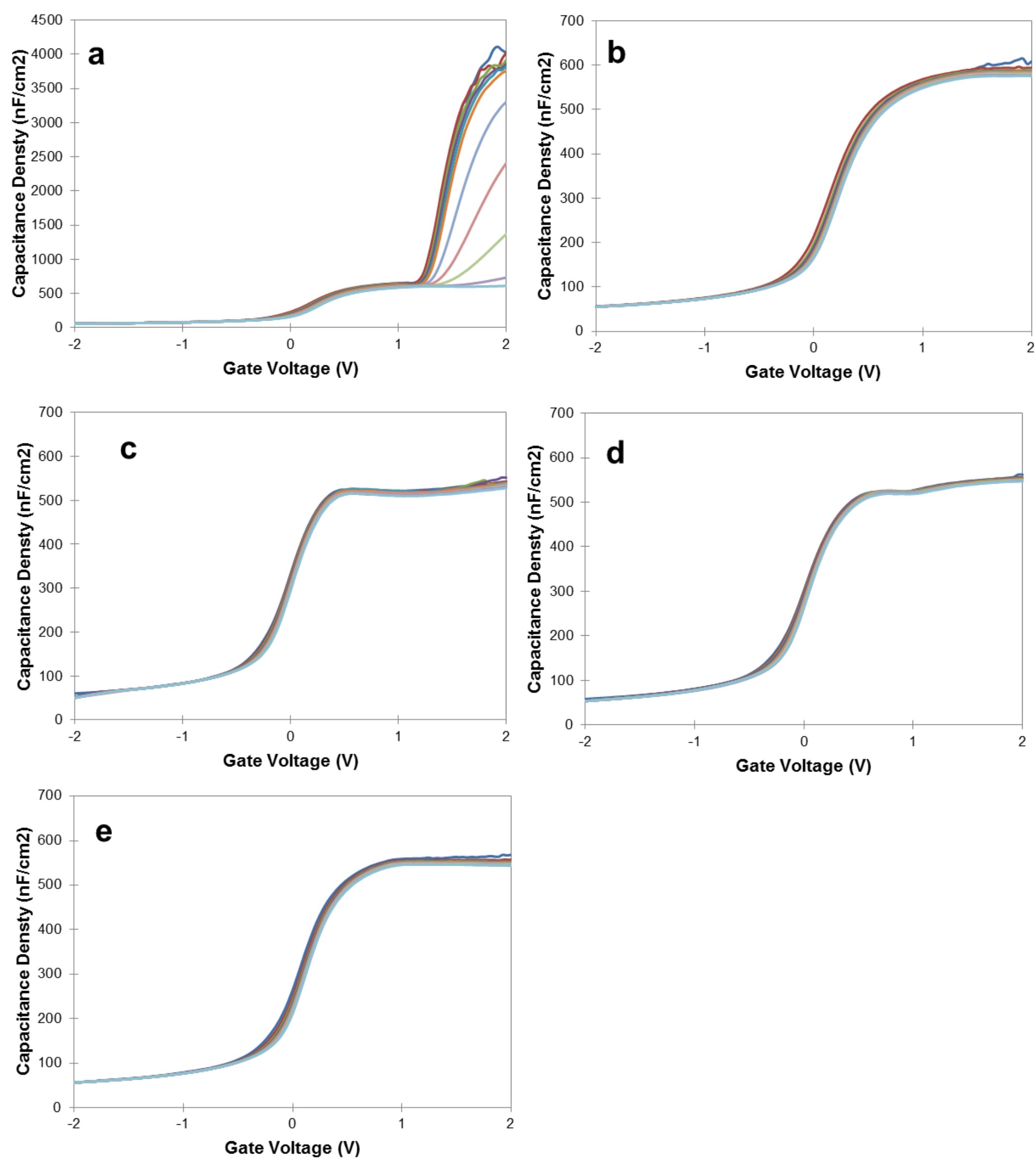

Figure 2.2. A study exploring the effects of TMA and water pulse lengths. C-V profiles measured from 1kHz-1Mhz for samples grown using a) 50ms TMA/50ms water, b) 200ms TMA/50ms water, c) 500ms TMA/50ms water, d) 200ms TMA/200ms water, and e) 200ms TMA/500ms water.

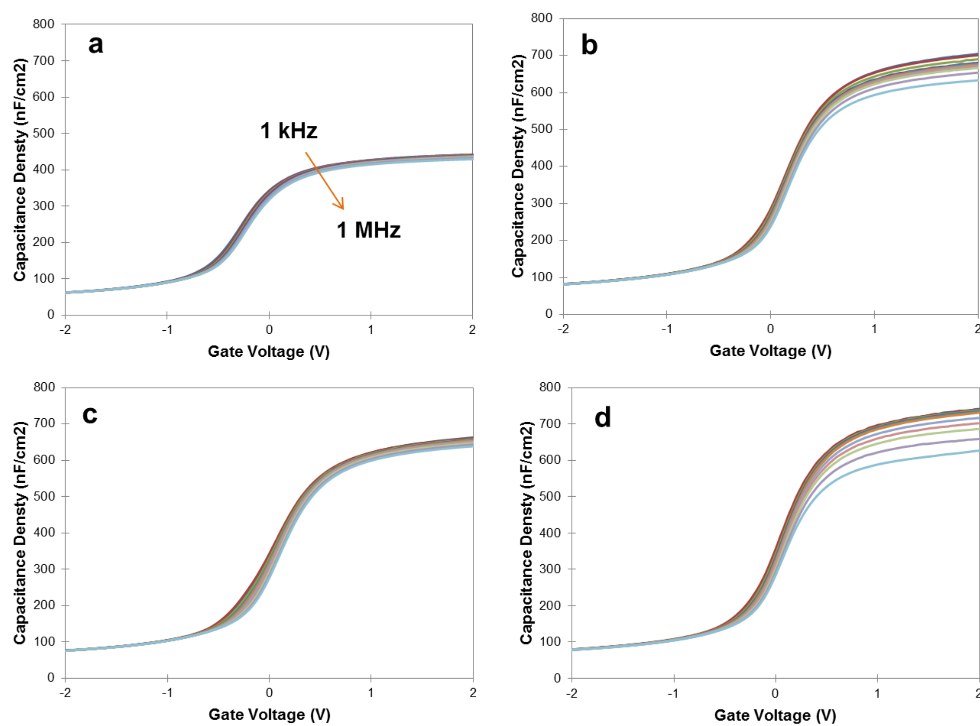

Figure 2.3. A study of the effects of purge time on the resulting film quality. ALD growth was performed using 5 cycles of TMA pretreatment followed by 80 cycles of TMA/H_2O using varying purge lengths. C-V profiles are shown for half-cycle purge times of a) 0.5 seconds, b) 2 seconds, c) 6 seconds, and d) 12 seconds.

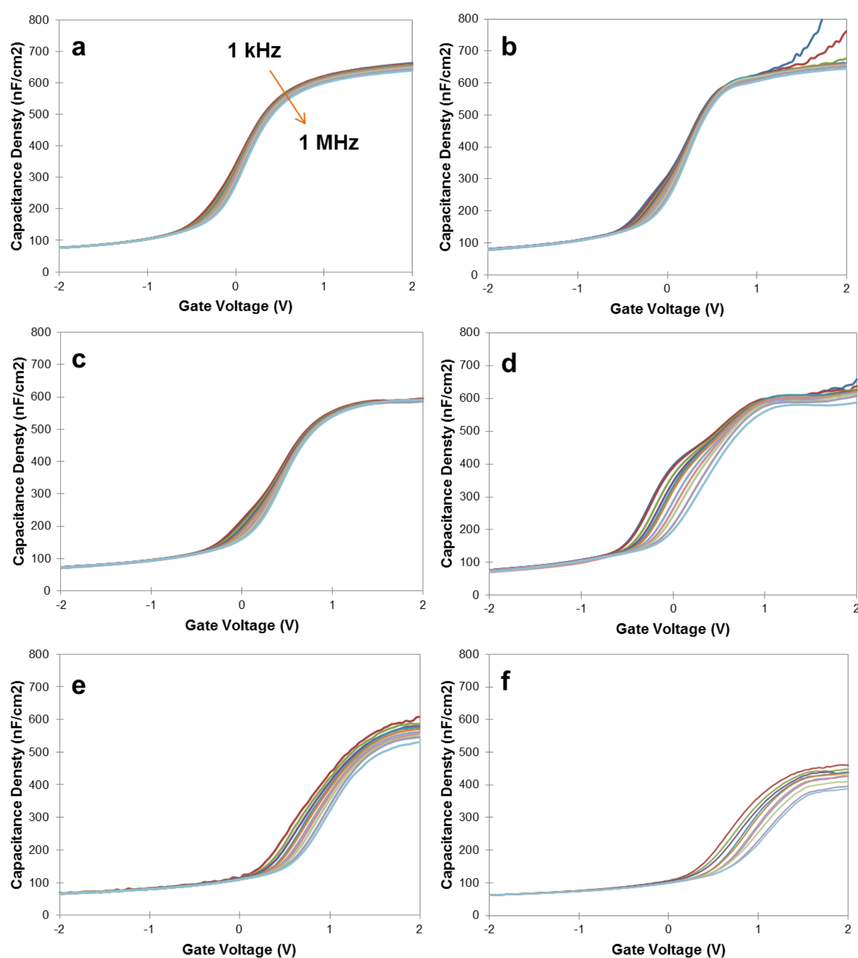

Figure 2.4. A study of the effects of hydrogen plasma power during the pretreatment on oxide quality. In-situ pretreatments using 5 cycles of H/TMA/H were performed at various hydrogen plasma powers and were followed by 80 cycles of ALD. C-V profile for a pretreatment of a) 5 cycles of TMA without the use of the hydrogen plasma. b) 5 cycles of H/TMA/H at a plasma power of 25W. c) 5 cycles of H/TMA/H at 50W plasma power. d) 5 cycles of H/TMA/H using 75W plasma power. e) 5 cycles of H/TMA/H using 100W plasma power. f) 5 cycles of H/TMA/H using 150W plasma power.

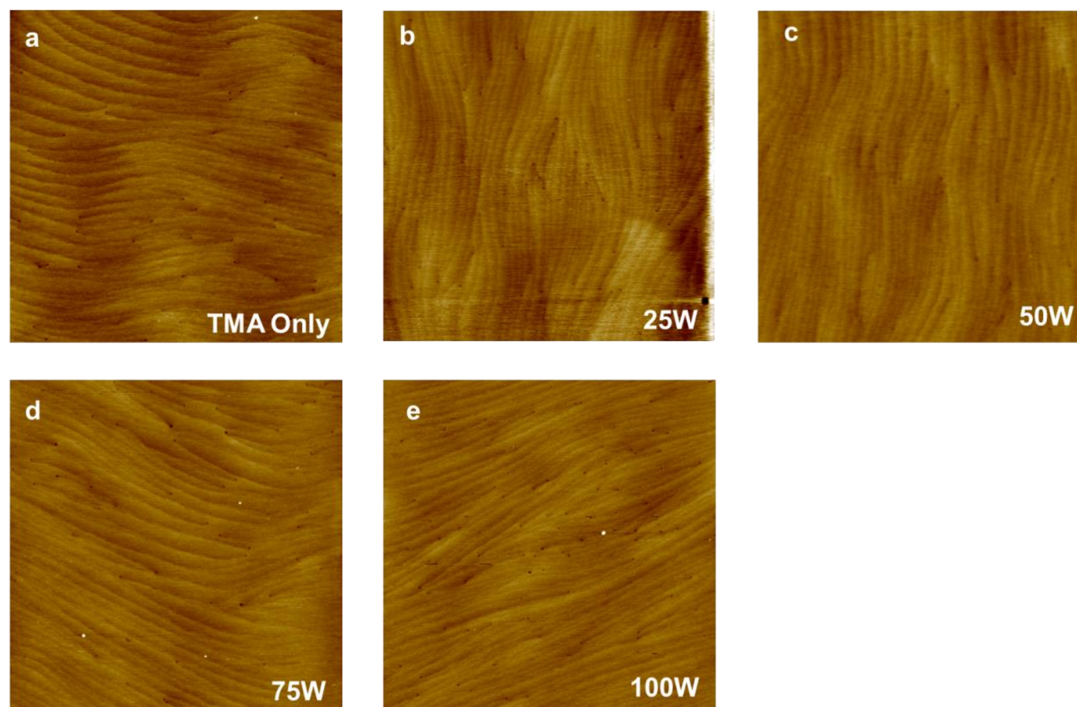

Figure 2.5. 5μm x 5μm AFM images of GaN surfaces treated with 5 cycles of H/TMA/H at varying plasma powers. The data scale is 10nm. a) No plasma, TMA only. b) 25W. c) 50W. d) 75W. e)100W. There are no discernable morphology changes due to plasma damage for any of the samples.

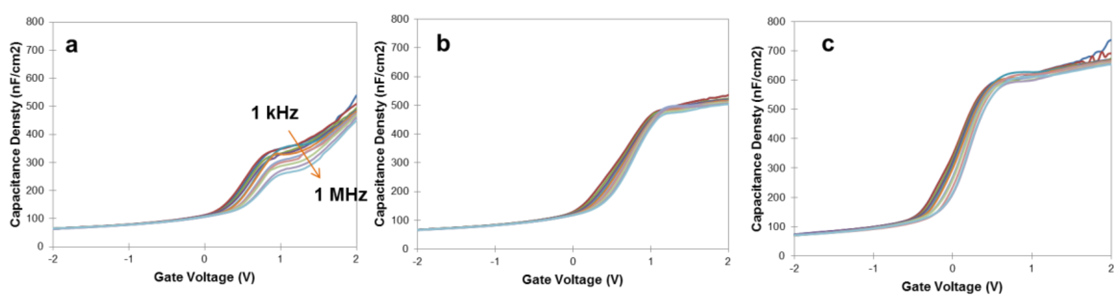

Figure 2.6. A study examining hydrogen plasma exposure times on the resulting film. C-V profiles for a) 2 cycles of H/TMA/H pretreatment, b) 5 cycles of H/TMA/H pretreatment, and c) 10 cycles of H/TMA/H pretreatment.

CHAPTER THREE

Preparation of Gallium Nitride Surfaces for Atomic Layer Deposition of Aluminum Oxide

3.1 Abstract

A combined wet and dry cleaning process for GaN(0001) has been investigated with XPS and DFT-MD modeling to determine the molecular-level mechanisms for cleaning and the subsequent nucleation of gate oxide ALD. *In-situ* XPS studies show that for the wet sulfur treatment on GaN(0001), sulfur desorbs at room temperature in vacuum prior to gate oxide deposition. Angle resolved depth profiling XPS post-ALD deposition shows that the a-Al_2O_3 gate oxide bonds directly to the GaN substrate leaving both the gallium surface atoms and the oxide interfacial atoms with XPS chemical shifts consistent with bulk-like charge. These results are in agreement with DFT calculations that predict the oxide/GaN(0001) interface will have bulk-like charges and a low density of band gap states. This passivation is consistent with the oxide restoring the surface gallium atoms to tetrahedral bonding by eliminating the gallium empty dangling bonds on bulk terminated GaN(0001).

3.2 Background

Gallium nitride (GaN) transistors support high power and high frequency operation. Typically, GaN transistors are depletion mode field-effect transistors that operate using Schottky gates, but high gate leakage and interest in creating enhancement mode transistors has prompted investigation into insulated gate structures[30, 48]. Insulated gate device performance is highly sensitive to defects in the

dielectric and at the insulator/semiconductor interface[49]. Without proper passivation, these defects can result in degradation of carrier mobility, anomalous time-dependence of device current, time-dependent breakdown, decrease in transconductance and pinning of the Fermi level[13]. Silicon nitride (Si_3N_4) is currently the standard for passivation of GaN surfaces because it readily forms an interface to GaN with good electrical properties[50, 51]. Unfortunately, the band offset of silicon nitride on GaN is relatively small due to its modest band gap (5eV), so the barrier to tunneling between the gate and channel is insufficient to significantly reduce leakage current when silicon nitride is used as a gate dielectric.

To reduce gate leakage, some groups have proposed alternative dielectrics such as Al_2O_3, Ta_2O_5, and SiO_2 which have larger band gaps[38, 52-54]. For this study, Al_2O_3 was chosen because it has a large conduction band offset with respect to GaN as well as a high permittivity (8-10) which allows for support of greater electric fields[54, 55]. Unfortunately, deposition of Al_2O_3 on air exposed GaN(0001) does not readily form a low-defect interface[55, 56]. Cleaning and preparation of the surface prior to oxide deposition is required to passivate interfacial defect states[55-57]. Studies have demonstrated success in removing the native oxide on GaN using various wet cleaning procedures[33, 34]. Additionally, there have been reports of improvement in oxide quality on GaN after exposure to trimethylaluminum (TMA) and atomic hydrogen prior to ALD deposition[45]. This effect is well documented on other III-V materials, as well[42, 58-60]. In this study, both *ex-situ* wet cleans and *in-situ* dry cleaning combinations were investigated to better understand the underlying atomic-level interactions at play.

Density functional theory (DFT) was used to predict the most stable state for several configurations of oxide-GaN(0001) interfaces as well as to illustrate the defect sites responsible for any interfacial trap states. To verify these models, an *ex-situ* wet clean using sulfur and *in-situ* dry cleaning with TMA and atomic hydrogen were performed, and the resulting interfaces characterized via XPS and capacitance-voltage profiling.

3.3 Experimental Modeling and Details

A. DFT-MD Modeling

To model both an ideal defect-free interface as well as the experimental interface, this study employed DFT with molecular dynamics (MD). Simulations were performed with the Vienna Ab-Initio Simulation Package (VASP) using projector augmented-wave (PAW) pseudopotentials and the Perdew-Burke-Ernzerhor (PBE) exchange correlation functional[61-65]. The amorphous Al_2O_3 model was generated in accordance with the method detailed by Chagarov[66]. After initial stacking of the a-Al_2O_3/GaN systems, they were partially relaxed for ~30 conjugate-gradient (CG) relaxation steps, annealed at 800K for 1000 fs with 1.0 fs timesteps, cooled to 0K for 200 fs, and finally relaxed below a 0.05 eV/Å force tolerance level. Three bottom layers of the GaN slab were permanently fixed in their bulk-like positions. Since the standard DFT PBE exchange-correlation functional underestimates the GaN band gap value, the PBE-relaxed systems were rescaled from PBE to HSE06 GaN lattice constant value and more accurate HSE06 hybrid-functional electronic structure was calculated[67-69].

B. Cleaning Study

Both *ex-situ* wet cleaning and *in-situ* dry cleaning methods were investigated to determine the effects on surface contamination and ALD nucleation density. Three sets of experiments were performed: X-ray photoelectron spectroscopy (XPS) of the surface after wet cleaning, XPS of the early stages of ALD deposition, and capacitance-voltage measurements of samples with a thicker oxide. For the first experiment, samples were exposed only to the wet clean process, and their surfaces probed with XPS for the presence of contamination or native oxide reformation. The second and third experiments included the addition of an *in-situ* dry cleaning process to the *ex-situ* wet cleaning.

All samples in this study were GaN(0001) grown via MOCVD on sapphire substrates, and for each of the three experiments every sample first received an *ex-situ* wet clean treatment. For step one of this wet treatment, all samples were first given an organic clean consisting of sequential dips in acetone, methanol, isopropanol, and deionized water. For step two, all samples received a dip in 6% $HCl_{(aq)}$ for 1 minute at room temperature. For step three, all samples were dipped in a 7% $NH_4OH_{(aq)}$ solution for 1 minute at room temperature. As shown by Hattori, the acid and base treatments ensured that the native oxide present on the air-exposed samples was removed[34]. After step three, two different treatments were tested with one group receiving a final dip in 5% $(NH_4)_2S_{(aq)}$ for 30 minutes at 50°C and the other group bypassing this treatment. The sulfur treatment is expected to prevent reoxidation in ambient during transfer to the vacuum ALD system consistent with experiments on

InGaAs[70, 71] and GaAs[72]. After each step, samples were rinsed in dionized water for 1 minute and then dried in N_2 gas.

For the first experiment, following the *ex-situ* wet clean, samples were immediately loaded into ultra-high vacuum at a base pressure of $2x10^{-10}$Torr. Following initial XPS measurements, samples were degassed in UHV at 130°C for 1 hour and subsequently annealed at 500°C for 30 minutes. The ramp rate for each thermal anneal was 1°C/min. Immediately after loading as well as following each degas and anneal step, samples were characterized using *in-situ* monochromatic XPS (XM 1000 MkII/SPHERA, Omicron Nanotechnology). The XPS was operated in constant analyzer energy mode with a pass energy of 50eV and beam width of 0.1eV using an Al Kα source. A detector angle of 30° with an acceptance of ±7° was used to maximize surface sensitivity. The spectrum analysis was performed using CASAXPS v2.3. The relative XPS intensity of each core peak (Ga, N, O, C, S) was obtained using Shirley fitting and dividing the calculated area under each peak by its Scofield XPS sensitivity factor.

For the second group of experiments investigating the early stages of ALD deposition, the samples were first treated using the wet organic, acid, base, and sulfur clean processes described above. The two groups of samples (with/without $(NH_4)_2S$ dip) were further divided based on two types of *in-situ* dry cleaning: those which received 5 cycles of TMA and those which received 5 cycles of atomic hydrogen/TMA/atomic hydrogen prior to the start of deposition which is identical to the *in-situ* H/TMA/H method reported by Son*l*[37]. In total, this produced four distinct combinations of wet and dry ALD pretreatments which have been denoted by letters

A-D. A summary of these treatments is shown in Table 1. The *in-situ* treatments were performed in the ALD chamber (Oxford Instruments FlexAl ALD) at a temperature of 300°C. For the pretreatments, each TMA cycle consisted of a 40ms pulse at a pressure of 200mTorr with Ar carrier gas flow of 100sccm followed by a 5 second Ar purge, and finally an H_2 gas stabilization step for 10 seconds[36 37]. Each atomic hydrogen pulse was generated using an Oxford FlexAl plasma source with an ICP forward power of 100W and consisted of exposure to the plasma for 2 seconds at an H_2 pressure of 20mTorr.

Table 3.1. Summary of ALD Pretreatments

Pretreatment	$(NH_4)_2S$ Wet Clean	TMA only	TMA and Atomic Hydrogen
A	No	Yes	No
B	Yes	Yes	No
C	No	No	Yes
D	Yes	No	Yes

Immediately following completion of each pretreatment, all samples received 8 cycles of ALD to deposit Al_2O_3 on the surface at 300°C using TMA as the metal precursor and water as the oxidant. The TMA half-cycle consisted of a 500ms TMA pulse at 20mTorr with an Ar carrier gas flow of 100sccm and a 7 second Ar purge at 200mTorr. Each oxidant half-cycle consisted of a 500ms water pulse at a pressure of 200mTorr with an Ar carrier gas flow of 250sccm which was followed by a 7 second Ar purge at 200mTorr. Between each half-cycle, the chamber was evacuated for 7 seconds and subsequently flushed with Ar for 7 seconds at 200mTorr.

To examine the state of interfacial bonding, Angle Resolved X-ray Photoelectron Spectroscopy (ARXPS) measurements were obtained using an XPS VG Theta Probe system with an Al Kα (1486.7eV) excitation. Samples were placed on the holder using Cu-Be pins as a support, pumped down in the load lock, and subsequently transferred into the chamber at a pressure of 3 x 10^{-9}Torr. Angle resolved spectra were obtained in the range of 26.75°-79.25° with a step size of 7.5°. The system was operated with a pass energy of 150eV. A 9.5eV flood gun was employed to compensate for the charging of samples.

For the final experiment, capacitance-voltage (C-V) measurements were performed using an Agilent B1500 Semiconductor Analyzer on samples which had the same four pretreatments A-D. In this case, however, a thicker oxide was required so the number of ALD cycles was increased from 8 to 80. The ALD process parameters are identical to those described above. The details of the (C-V) measurements have been outlined in a separate study.

3.4 Results and Discussion

A. DFT Modeling

Most GaN transistors have n-type channels since they are used in power devices, so defect states near the conduction band edge or mid-gap position are of the greatest concern. Therefore, a successful pre-ALD cleaning procedure for GaN devices would need to passivate the defects responsible for these trap states. To identify the source of problematic interface states in the amorphous Al_2O_3/GaN system, DFT calculations were performed to obtain the density of states and band-

decomposed charge density fields for the bulk-terminated surface, a-Al_2O_3 bonded to a layer of crystalline Ga_2O_3[73], and a-Al_2O_3 bonded directly to the Ga-polar GaN(0001) surface. Calculations for the N-polar GaN($000\bar{1}$) surface were also performed, and the results can be found in the supplemental materials[74]. The final state of each system was determined using DFT-MD annealing, cooling, and final relaxation. This allowed for the analysis of an amorphous oxide layer at finite temperature as it relaxed to its most stable state.

Feenstra prepared a nearly ideal oxide/GaN stack by *in-situ* thermal oxidation of the gallium ad-layer on GaN(0001) MBE grown samples. Both scanning tunneling microscopy (STM) and low energy electron diffraction (LEED) showed the surface oxide layer to be crystalline, and scanning tunneling spectroscopy (STS) showed the surface Fermi level to be unpinned[73]. The experimental unit cell is too large to be modeled using a full oxide stack, so a simplified model was employed substituting an O-Ga-O layer with approximately the same structure as GaN. On top of the crystalline O-Ga-O layer, amorphous oxide was bonded and annealed at 800K for 1000fs with 1.0fs timesteps, cooled to 0K for 200fs, and finally relaxed below 0.05 eV/Å force tolerance-level using DFT-MD. The total system consists of 174 atoms. The annealed/relaxed structure is shown in Fig. 1 along with the corresponding density of states (DOS). The model shows the interface is not quite ideal since there are a few under-coordinated atoms at the a-Al_2O_3/O-Ga-O interface and within the O-Ga-O layer. The under-coordinated oxygen atom is denoted by a blue arrow while the under-coordinated gallium atom is denoted by a red arrow. The gallium and oxygen dangling bonds normally produce states within the bulk band gap, but since these under-

coordinated atoms are in a wide band gap oxide layer they may not produce states inside the band gap of the full a-Al_2O_3/O-Ga-O/GaN stack. States outside the GaN band gap will have minimal effect on device performance.

The HSE DOS shows that the annealed structure has only three small mid-gap states, which are indicated in Fig. 1b as A, B, and C. To determine whether any of these states were the result of the two under-coordinated atoms present in the model, the band decomposed charge densities were calculated for states A-C. The results of these calculations are shown in Fig. 1c-e with regions of highest charge density highlighted in purple. The band decomposed charge density for valence band state A is delocalized among all the N atoms except those at the interface. Both the band decomposed charge density in Fig. 1c and the comparison to the bulk DOS in Fig. 1b show it is a bulk state. The band decomposed charge density for conduction band state B (Fig. 1d) is also delocalized, but in this case is distributed across oxygen atoms in the crystalline O-Ga-O layer without significant concentration on the under-coordinated atoms. Again, this state is not caused by aberrant interfacial bonding or the presence of the under-coordinated atoms. The band decomposed charge density for the final state, C, is centered on atoms at the vacuum/a-Al_2O_3 interface. This state arises due to limitations of the DFT vacuum/oxide passivation technique and is therefore inconsequential. Overall, the band decomposed charge density breakdowns show no mid-gap states resulting from aberrant bonding at any interface. This is consistent with defects in the O-Ga-O layer producing states outside the GaN band gap.

To understand how the O-Ga-O layer is able to passivate the interface, a Bader charge analysis was performed. Gallium atoms from the O-Ga-O layer have -0.32 (from -0.36 to -0.29) lower Bader charge values (more positive) than those in bulk GaN. These results suggest that Ga atoms the O-Ga-O layer have charge similar to Ga in bulk GaN. Because the gallium in the O-Ga-O layer is bulk-like, these bonds produce states very similar to bulk GaN therefore resulting in a clean band gap.

For comparison to the crystalline interlayer O-Ga-O case and to serve as a model for the experimental results in this paper, simulations were performed for an amorphous Al_2O_3 layer bonded directly to Ga-terminated GaN(0001). As indicated by the arrows in Fig. 2a, the annealed a-Al_2O_3/GaN(0001) simulation has three defective sites—a Ga atom with a dangling bond (red arrow) and two Ga-Al metal-metal bonds (blue arrows). While the dangling bonds in the O-Ga-O layer in Fig. 1 are in a wide band gap oxide, the dangling bond and metallic bonds in the Fig. 2 system are located directly on the semiconductor. Unlike those in the wide band gap oxide, the aberrant bonds in this case are expected to create states in the band gap.

Fig. 2b compares the DOS for the a-Al_2O_3/GaN(0001) stack with that of the bulk GaN and clean unpassivated bulk terminated GaN(0001). The DOS shows that while the a-Al_2O_3/GaN(0001) passivated many of the mid gap states of clean GaN(0001), there are band gap states on a-Al_2O_3/GaN(0001) which are not present in bulk GaN(0001). To determine if the band gap states of a-Al_2O_3/GaN(0001) originate at interfacial defects, band- decomposed charge densities were calculated for the three states denoted by arrows in Fig 2b. Band-decomposed charge simulations show that the two Ga-Al metal-metal bonds (blue arrows) are responsible for the valence band

edge states A, while the gallium dangling bond is the origin of the conduction band edge states B and C. The results are consistent with the need to passivate all dangling bonds and remove all metallic bonds which are directly on the GaN(0001) surface.

To understand how the Al_2O_3 passivates the GaN(0001) (except for the metallic and dangling bonds), a Bader charge analysis was performed comparing interfacial atoms to their respective bulk counterparts. Bader charge calculations for a-Al_2O_3/GaN(0001) indicated interfacial aluminum atoms have nearly bulk-like bonding as interfacial aluminum atoms have only +0.02 |e| (from 0.0 to +0.03) higher Bader charges (more negative) than those in bulk a-Al_2O_3. Along the same lines, interfacial oxygen atoms have -0.12 |e| (from -0.08 to -0.18) lower Bader charges (more positive) than oxygen atoms in bulk a-Al_2O_3. The interfacial gallium atoms (except the two Ga's bonded to Al) have deviations of only -0.01 |e| (-0.11 to +0.22) compared to gallium in bulk GaN. However, the two gallium atoms belonging to the Ga-Al bonds have Bader charge deviations of +0.94 and +0.96 (more negative), and the gallium atom not forming a bond to the oxide has a Bader charge deviation of +0.22 (more negative). This shows that for the conduction band edge states on the gallium atom with a dangling bond, a state forms in the band gap due to the weak binding of electrons in the dangling bond instead of aberrant charge. The presence of strong, ionic Ga-O bonds in the a-Al_2O_3/O-Ga-O/GaN(0001) model shifts gallium dangling bond states to energies outside the band gap while in the case of a-Al_2O_3 directly bonded to GaN(0001), the covalent bonding to the GaN bulk creates dangling bonds with states that exist within the bulk band gap. Despite the formation of these sites, the Al_2O_3 still passivates most states and results in a relatively clean band gap.

To obtain complete passivation, ALD will need to be nucleated in every unit cell to insure all dangling bonds are eliminated.

B. Cleaning Study

To understand the mechanisms of contamination removal and gallium dangling bond passivation, a two-part cleaning process was employed consiting of an *ex-situ* wet clean and an *in-situ* dry clean performed immediately prior to ALD of Al_2O_3. The first portion of the study examined the wet clean alone to determine its effect on the state of the surface. The XPS data shown in Fig. 3 compares the oxygen and carbon coverage on the GaN(0001) surface for samples having received one of three *ex-situ* wet cleans and having no UHV annealing or UHV annealing at 130°C or 500°C. The coverages of oxygen and carbon have been normalized to the total gallium signal. The control samples, which received only the organic solvent degrease, served to establish a baseline for the initial condition of the surface.

The unannealed organic solvent cleaned samples show a 50% oxygen and 100% carbon coverage (normalized to Ga) (Fig 3a). For the samples cleaned using the 6%HCl and 7%NH_4OH solutions, the coverage of surface contaminants was reduced to approximately 30% oxygen and 50% carbon. For the samples which also received the 5%$(NH_4)_2S$(aq) treatment, the amount of oxygen and carbon on the surface was further reduced to 10% oxygen and 30% carbon.

To determine if just *in-situ* annealing could remove residual carbon and oxygen contamination at typical ALD temperatures, annealing was performed at both 130°C (Fig. 3b) and 500°C (Fig 3c). Annealing to 130°C, which is a standard degas

temperature for driving off physisorbed water and other weakly bound adsorbates such as small hydrocarbons, had almost no effect on either the carbon or oxygen ratios. Annealing to 500°C, the limit for most ALD chambers, significantly reduced the amount of oxygen. (Note 500°C is well above the temperature at which ALD precursor act as CVD precursors). The oxygen ratio for all samples, regardless of wet clean, was reduced to approximately 5% after the 500°C anneal, which is near the sensitivity limit for the XPS system. However, after the 500°C anneal, the carbon remained unchanged. A UHV anneal at 300°C (the temperature of the ALD performed in this study) was performed on samples having received the full sulfide clean (results not shown). This data appeared nearly identical to that obtained from the 500°C anneal. This indicates that the majority of residual oxide is removed below the temperature at which ALD was performed for this study. This also indicates that additional cleaning is necessary to remove the residual carbon. This is critical as TMA will not nucleate on the portions of the surface which are covered by carbon. Therefore, a thicker oxide must be subsequently deposited to grow over the unreacted sites leaving defects at the interface.

The lower coverages of oxygen and carbon in unannealed samples treated with 5% $(NH_4)_2S$ compared to samples which only received the HCl and NH_4OH clean suggests that the $(NH_4)_2S$ solution protects the surface from reoxidation. $(NH_4)_2S$ is known to form a stable sulfur layer on GaAs[47, 72, 75, 76]. XPS measurements were performed on GaN(0001) and GaAs(001) samples which received the identical $(NH_4)_2S$ wet clean process. The samples were measured at room temperature immediately after loading into the chamber. A comparison between the room

temperature results for the GaAs and GaN samples is shown in Fig. 4. These XPS results show a clear sulfur peak for the GaAs sample which had received the $(NH_4)_2S$ treatment while that same peak is missing for GaN. In the case of GaN, the bonding between the sulfur and GaN is sufficiently weak to allow for immediate desorption in vacuum consistent with the sulfur layer only being stable in the presence of a moist atmosphere.

To experimentally verify the DFT-MD results and examine the effects of the wet and dry cleaning processes on the bonding at the oxide-semiconductor interface, Angle Resolved XPS (ARXPS) was performed on Ga-terminated GaN(0001) samples that underwent 8 cycles of Al_2O_3 ALD. Spectra were taken at a range of exit angles to examine the chemical shifts as the structure transitions from bulk GaN to the Al_2O_3/GaN interface. The spectra for the Ga 3d peak of the control sample (treatment A) and one which received both the $(NH_4)_2S$ *ex-situ* and the *in-situ* cyclic TMA and hydrogen clean (treatment D) are shown in Fig. 5. In the spectra, the intensity of the Ga 3d peak increases as the collection angle becomes more bulk sensitive, but there is no discernible chemical shift. This indicates that the bulk and surface gallium atoms have identical charge states. This is consistent with the DFT-MD model for the a-Al_2O_3/GaN(0001) interface, since the Bader charge calculations show the interfacial, fully bonded Gallium atoms are in a nearly bulk-like state. The calculated difference of -0.01 |e| in charge between bulk and interfacial atoms is essentially negligible and would not produce a chemical shift detectable by XPS.

Reports in the literature suggest that the difference in charge from bulk GaN to Ga_2O_3 would produce a shift large enough to be detected in the XPS scans. Wolter

determined that Ga 3d states in Ga_2O_3 have a chemical shift of +1.2 eV on GaN[77]. Surdu-Bob determined the Ga3d chemical shift of gallium suboxide Ga_2O relative to Ga_2O_3 of -0.6 eV. Therefore, it is estimated that Ga_2O has a chemical shift of +0.6 eV relative to bulk GaN[78]. The results of Woter and Surdu-Bob show that XPS should readily detect any interfacial oxide or suboxide formation. Thus, the absence of any chemical shift in the spectra for the Ga 3d peak indicates that there is not significant formation of Ga_2O_3 or Ga_2O, and that the combined *ex-situ* and *in-situ* cleaning process have restored the interfacial atoms to a bulk-like configuration. Furthermore, this result is in agreement with the DFT-MD model presented in this work, thus confirming its validity.

Table 3.2. Summary of Trap Densities

Pretreatment	**D_{it} ($eV^{-1}cm^{-2}$)**	**Border Traps ($eV^{-1}cm^{-3}$)**
A (TMA Only)	$2.8\times10^{12} \pm 1.3\%$	$2.0\times10^{20} \pm 5.1\%$
B (Sulfide + TMA)	$2.0\times10^{12} \pm 4.1\%$	$1.0\times10^{20} \pm 2.8\%$.
C (Hydrogen and TMA)	$1.1\times10^{12} \pm 4.1\%$	$3.9\times10^{19} \pm 4.5\%$
D (Sulfide + Hydrogen and TMA)	$0.9\times10^{12} \pm$ 4/1%	$2.5\times10^{19} \pm 1.3\%$

[1]Trap densities (D_{it}) were calculated using the Terman Method, at an energy corresponding to 0.5eV below the conduction band edge. Border traps were evaluated in the accumulation region of the C-V curves.
[2]Error reported is the relative standard error of the mean.

In a separate study[79], ALD pretreatments A-D described previously were applied prior to deposition of 80 cycles of Al_2O_3 gate oxide. Capacitance-voltage (C-V) measurements were employed to determine the effect of the pretreatments of electronic defect states. Interfacial trap densities were calculated using the Terman method and border trap densities in the oxide were quantified using the method

detailed by Taur[39, 45]. A summary of these results is listed in Table 3.2. The calculations showed that samples that had pretreatments C and D, which included atomic hydrogen in the *in-situ* clean, had the lowest densities of both interfacial traps and border traps. The addition of the sulfur treatment resulted in further, more modest reductions in trap density. One-way anova model p-value calculations for a sample of devices produced using each pretreatment confirms that the reductions in both D_{it} and border trap densities between samples with treatments C and D are significant. Overall, these results indicate that the ALD pre-clean process improves the quality of the deposited oxide. More specifically, the reduction in trap density is consistent with an increase in nucleation density, which would result in passivation of the aberrant interfacial bonds that produce trap states.

3.5 Conclusion

Theoretical DFT modeling predicts that gate oxide stacks consisting of a-Al_2O_3/O-Ga-O/GaN(0001) will produce a nearly ideal interface because the crystalline O-Ga-O layer eliminates all dangling bonds on GaN(0001) and dangling bond defects at the Al_2O_3/O-Ga-O interface have states outside the band gap of GaN(0001). DFT models of a simpler structure, a-Al_2O_3/GaN(0001), in which the amorphous oxide bonds directly to GaN(0001) have an interface with a slightly greater propensity to form defects than a-Al_2O_3/O-Ga-O/GaN(0001). However, a-Al_2O_3 does passivate the GaN(0001) interface if the oxide nucleates in each unit cell and Ga-Al bonds and GaN dangling bonds are eliminated. The a-Al_2O_3 layer is able to passivate GaN(0001) because the oxide removes the dangling bond states from the surface gallium atoms

and restores their bulk-like charge. In contrast to the O-Ga-O/GaN(0001) interface, the dangling and metallic bonds in the direct bonding configuration create mid-gap states because of the relative weakness of bonds in GaN compared to O-Ga-O. To nucleate the bonding in each unit cell, the interface must be free of contamination prior to Al_2O_3 ALD deposition. XPS results showed that the use of a 5%$(NH_4)_2S$ after wet etch removal of the native oxide successfully reduced carbon and oxygen contamination as well as prevented reoxidation of the surface prior to loading into the ALD chamber. In contrast to S/InGaAs(001), the sulfur on GaN(0001) desorbs even at 25°C XPS experiments show bulk-like bonding at the a-Al_2O_3/GaN(0001) interface consistent with DFT models of the Al_2O_3/GaN(0001) interface.

3.6 Acknowledgements

The authors would like to thank the SRC-Least program (section and theme 2383.001), Office of Naval Research (N00014-45-4-0078), and the National Science Foundation (NSF DMR 1207213) for their generous support of this research.

3.7 Figures

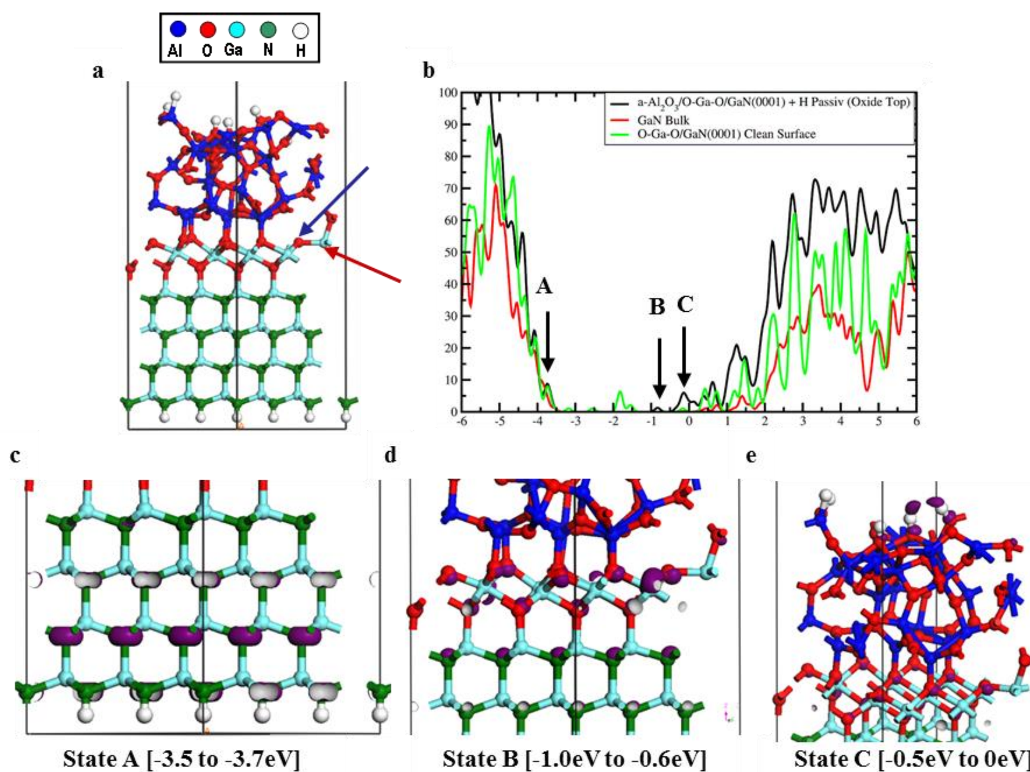

Figure 3.1. a-Al_2O_3/ordered O-Ga-O interlayer/GaN(0001) a) DFT model of annealed and relaxed amorphous Al_2O_3 on an ordered O-Ga-O interlayer on GaN(0001) surface. Undercoordinated oxygen and gallium atoms are denoted by blue and red arrows, respectively. b) The HSE density of states for the a-Al_2O_3/O-Ga-O/GaN(0001), O-Ga-O/GaN(0001) without Al_2O_3 passivation, and GaN bulk systems. States within the bulk band gap have been highlighted by arrows A-C. c) The decomposed charge density for state A. The valence band edge state, A, is a delocalized bulk state and therefore not important. d) The decomposed charge density for state B. The conduction band edge state, B, is on the N atoms near the O-Ga-O/GaN interface as well as oxygen atoms within the O-Ga-O layer. The undercoordinated oxygen and gallium atoms in the ordered O-Ga-O layer do not contribute to the B state. (e) The decomposed charge density for state C. The conduction band edge state, C, is mostly at the vacuum/Al_2O_3 interface and is therefore not important.

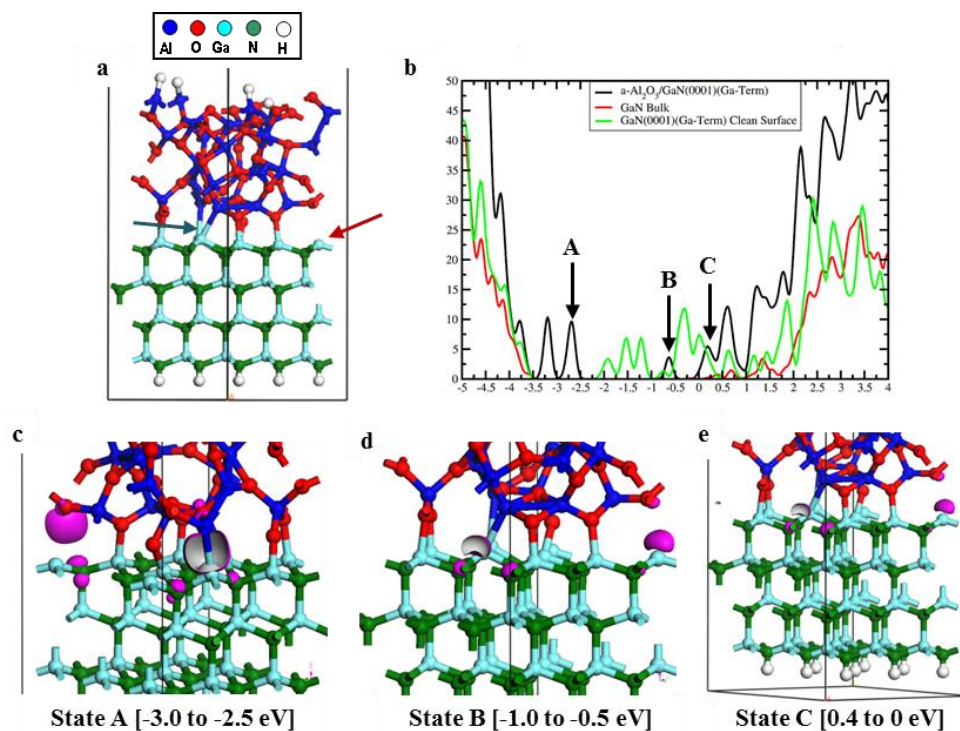

Figure 3.2. a-Al_2O_3/GaN(0001). a) Model of amorphous a-Al_2O_3 bonded directly to Ga-polar GaN(0001). The blue arrows highlight two metallic Ga-Al bonds and a red arrow highlights an undercoordinated Ga atom. b) The HSE density of states for a-Al_2O_3/GaN(0001), unpassivated GaN(0001), and bulk GaN. The arrows designate states which exist within the bulk band gap. The a-Al_2O_3 has passivated most of the surface states on the clean Ga-polar GaN(0001) surface (black line). c) The band decomposed charge densities of valence band edge state A. The states are concentrated on the Ga-Al metallic bonds (blue arrow in 2a). d) The band-decomposed charge densities of conduction band edge state B, which originates on an under-coordinated Ga atom (red arrow in 2a). e) The band-decomposed charge density of valence band edge state C, which is caused by the presence of undercoordinated Ga atoms (red arrow in 2a).

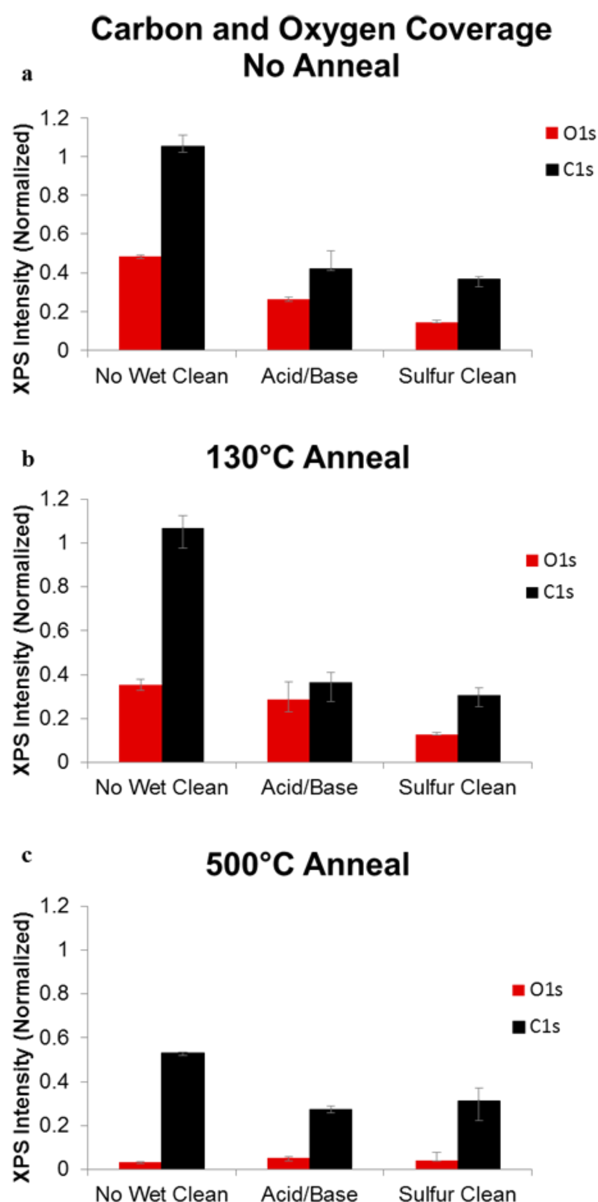

Figure 3.5. *In-situ* XPS study of the effect of annealing on wet cleaned GaN(0001). Carbon and oxygen coverage for samples UHV annealed at a) no anneal (room temperature), b) 130°C, and c) 500°C. Without annealing, the addition of the HCl and NH_4OH cleans reduced the carbon and oxygen contamination to 40% and 25%, respectively. The $(NH_4)_2S$ treatment reduced the oxygen coverage to approximately 10% but had only a small effect on surface carbon. The 130°C anneal resulted in very little change compared to no anneal. After annealing at 500°C, the oxygen coverage was reduced to approximately 5% while the carbon coverage remained unchanged. The error bars reflect the range of values obtained from multiple fittings of the XPS spectra.

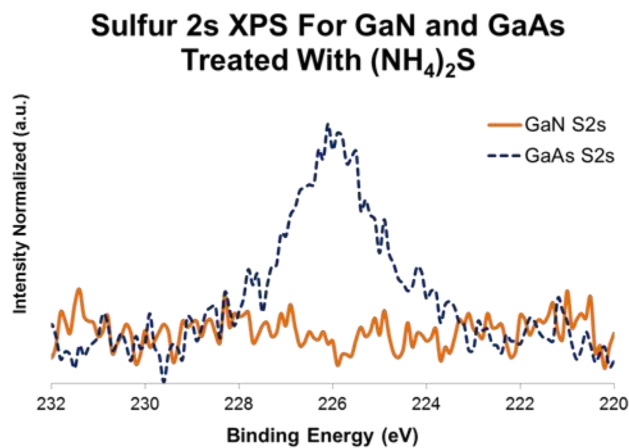

Figure 3.4. In_Situ XPS study of a sulfur 2s GaN(0001) and GaAs(001) treated with $(NH_4)_2S$. Both measurements were taken immediately after loading into the vacuum chamber at room temperature. The GaAs sample which has a S peak while the GaN does not have an S peak received the $(NH_4)_2S$ treatment. The bonding between the sulfur and GaN is sufficiently weak to allow for immeadiate desorption in vacuum.

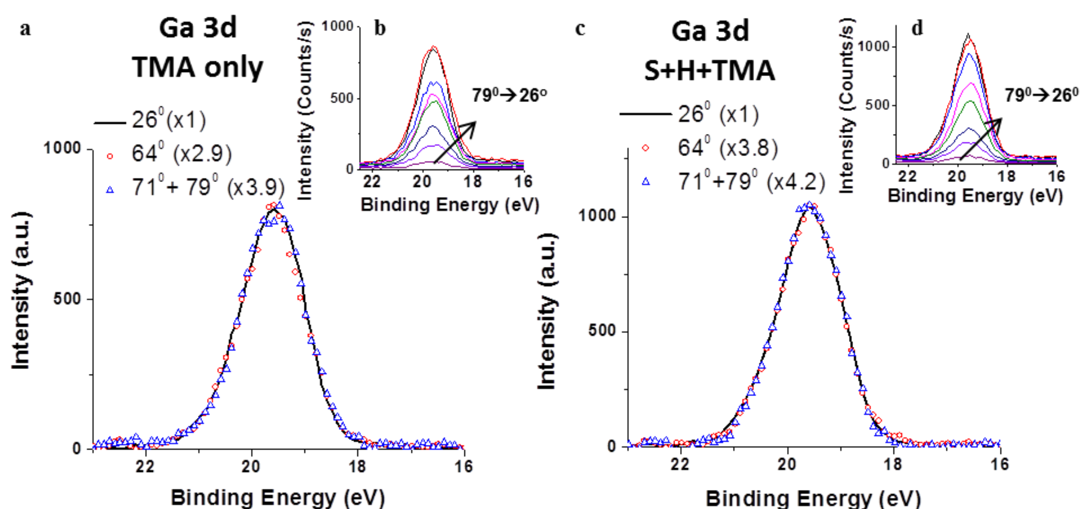

Figure 3.5. *Ex-situ* angle resolved XPS of a-Al_2O_3/GaN(0001) stack. a) Ga 3d XPS spectra at varying collection angles with respect to the surface normal of the control sample treated with TMA only (treatment A). The curves corresponding to near normal emission (26^0) and near grazing emission (64^0 and combined 71^0 with 79^0 spectra) are extracted from (b) experimental angle-resolved spectra by background subtraction and scaling with the factors shown in brackets. c) and d) Similar spectra for the sample treated with the $(NH_4)_2S$ wet clean as well as cyclic TMA and hydrogen (treatment D). There is no change in the peak energy position versus angle consistent with the absence of a detectable amount of interfacial gallium oxide. The scaling factors for the grazing emission spectra are higher for the spectra c-d that is the result of a thicker a-Al_2O_3 after treatment D.

REFERENCES

1. U. K. Mishra, P. Parikh and Y.-F. Wu, PROCEEDINGS-IEEE **90** (6), 1022-1031 (2002).

2. J. Kuzmik, Electron Device Letters, IEEE **22** (11), 510-512 (2001).

3. W. Yi-Feng, D. Kapolnek, J. P. Ibbetson, P. Parikh, B. P. Keller and U. K. Mishra, Electron Devices, IEEE Transactions on **48** (3), 586-590 (2001).

4. L. Shen, S. Heikman, B. Moran, R. Coffie, N. Q. Zhang, D. Buttari, I. P. Smorchkova, S. Keller, S. P. DenBaars and U. K. Mishra, Electron Device Letters, IEEE **22** (10), 457-459 (2001).

5. J. A. del Alamo and J. Joh, MiRe **49** (9–11), 1200-1206 (2009).

6. P. D. Ye, B. Yang, K. K. Ng, J. Bude, G. D. Wilk, S. Halder and J. Hwang, Applied Physics Letters **86** (6), 063501-063501-063503 (2005).

7. Y. Hao, Y. Ling, M. Xiaohua, M. Jigang, C. Menyi, P. Caiyuan, W. Chong and J. Zhang, Electron Device Letters, IEEE **32** (5), 626-628 (2011).

8. C. Liu, E. F. Chor and L. S. Tan, Semicond. Sci. Technol. **22** (5), 522 (2007).

9. J. Kuzmik, G. Pozzovivo, S. Abermann, J.-F. Carlin, M. Gonschorek, E. Feltin, N. Grandjean, E. Bertagnolli, G. Strasser and D. Pogany, Electron Devices, IEEE Transactions on **55** (3), 937-941 (2008).

10. W. B. Lanford, T. Tanaka, Y. Otoki and I. Adesida, Electron. Lett **41** (7), 449-450 (2005).

11. W. Ronghua, P. Saunier, X. Xiu, L. Chuanxin, G. Xiang, G. Shiping, G. Snider, P. Fay, D. Jena and X. Huili, Electron Device Letters, IEEE **31** (12), 1383-1385 (2010).

12. T. Zimmermann, D. Deen, Y. Cao, J. Simon, P. Fay, D. Jena and H. Grace Xing, Electron Device Letters, IEEE **29** (7), 661-664 (2008).

13. D. Segev and C. Van de Walle, EPL (Europhysics Letters) **76** (2), 305 (2006).

14. S. M. George, Chem. Rev. **110** (1), 111-131 (2009).

15. R. Katamreddy, Z. Wang, V. Omarjee, P. V. Rao, C. Dussarrat and N. Blasco, ECS Transactions **25** (4), 217-230 (2009).

16. M. Ritala and J. Niinistö, ECS Transactions **25** (8), 641-652 (2009).

17. R. K. Kanjolia, J. Anthis, R. Odedra, P. Williams and P. Heys, ECS Transactions **16** (4), 79-86 (2008).

18. B. Lee, K. Choi, A. Hande, M. Kim, R. Wallace, J. Kim, Y. Senzaki, D. Shenai, H. Li and M. Rousseau, Microelectron. Eng. **86** (3), 272-276 (2009).

19. F. T. Edelmann, Chem. Soc. Rev. **38** (8), 2253-2268 (2009).

20. R. L. Puurunen, J. Appl. Phys. **97** (12), - (2005).

21. M. Leskelä and M. Ritala, Thin Solid Films **409** (1), 138-146 (2002).

22. J. W. Elam, M. D. Groner and S. M. George, Rev. Sci. Instrum. **73** (8), 2981-2987 (2002).

23. R. Wind and S. George, J.Phys. Chem. A **114** (3), 1281-1289 (2009).

24. A. Delabie, S. Sioncke, J. Rip, S. Van Elshocht, G. Pourtois, M. Mueller, B. Beckhoff and K. Pierloot, J. Vac. Sci. Tech. A **30** (1), (2012).

25. A. W. Ott, J. W. Klaus, J. M. Johnson and S. M. George, Thin Solid Films **292** (1–2), 135-144 (1997).

26. A. C. Dillon, A. W. Ott, J. D. Way and S. M. George, Surf. Sci. **322** (1–3), 230-242 (1995).

27. J. S. Lee, T. Kaufman-Osborn, W. Melitz, S. Lee, A. Delabie, S. Sioncke, M. Caymax, G. Pourtois and A. C. Kummel, The J. of Chem. Phys. **135** (5),)2011).

28. S. D. Elliott and J. C. Greer, J. Mater. Chem. **14** (21), 3246-3250 (2004).

29. Y. Widjaja and C. B. Musgrave, Appl. Phys. Lett. **80** (18), 3304-3306 (2002).

30. K. Matocha, T. P. Chow and R. J. Gutmann, Electron Devices, IEEE Transactions on **52** (1), 6-10 (2005).

31. H. Wang, J. W. Chung, X. Gao, S. Guo and T. Palacios, physica status solidi (c) **7** (10), 2440-2444 (2010).

32. N. Nepal, N. Y. Garces, D. J. Meyer, J. K. Hite, M. A. Mastro and C. R. Eddy Jr, Applied physics express **4** (5), 055802 (2011).

33. A. N. Hattori, K. Endo, K. Hattori and H. Daimon, Appl. Surf. Sci. **256** (14), 4745-4756 (2010).

34. A. N. Hattori, F. Kawamura, M. Yoshimura, Y. Kitaoka, Y. Mori, K. Hattori, H. Daimon and K. Endo, Surf. Sci. **604** (15), 1247-1253 (2010).

35. S. King, J. Barnak, M. Bremser, K. Tracy, C. Ronning, R. Davis and R. Nemanich, J. Appl. Phys. **84** (9), 5248-5260 (1998).

36. V. Chobpattana, J. Son, J. J. Law, R. Engel-Herbert, C.-Y. Huang and S. Stemmer, Applied Physics Letters **102** (2), 022907-022907-022903 (2013).

37. J. Son, V. Chobpattana, B. M. McSkimming and S. Stemmer, Applied Physics Letters **101** (10), 102905 (2012).

38. S. Gu, H. Katayose, K. Nomoto, T. Nakamura, A. Ohoka, K. Lee, W. Lu and P. M. Asbeck, physica status solidi (c) **10** (5), 820-823 (2013).

39. Y. Yuan, L. Wang, B. Yu, B. Shin, J. Ahn, P. C. McIntyre, P. M. Asbeck, M. J. Rodwell and Y. Taur, IEDL **32** (4), 485 (2011).

40. A. Ali, H. Madan, S. Koveshnikov, S. Oktyabrsky, R. Kambhampati, T. Heeg, D. Schlom and S. Datta, Electron Devices, IEEE Transactions on **57** (4), 742-748 (2010).

41. M. Milojevic, F. S. Aguirre-Tostado, C. L. Hinkle, H. C. Kim, E. M. Vogel, J. Kim and R. M. Wallace, Appl. Phys. Lett. **93** (20), - (2008).

42. C. L. Hinkle, A. M. Sonnet, E. M. Vogel, S. McDonnell, G. J. Hughes, M. Milojevic, B. Lee, F. S. Aguirre-Tostado, K. J. Choi, H. C. Kim, J. Kim and R. M. Wallace, Appl. Phys. Lett. **92** (7), 071901 (2008).

43. R. M. Wallace, ECS Transactions **16** (5), 255-271 (2008).

44. S. Klejna and S. D. Elliott, J. Phys. Chem. C **116** (1), 643-654 (2011).

45. B. Brennan, X. Qin, H. Dong, J. Kim and R. M. Wallace, Applied Physics Letters **101** (21), 211604 (2012).

46. M. Milojevic, C. L. Hinkle, F. S. Aguirre-Tostado, H. C. Kim, E. M. Vogel, J. Kim and R. M. Wallace, Appl. Phys. Lett. **93** (25), - (2008).

47. M. Milojevic, C. L. Hinkle, F. S. Aguirre-Tostado, H. C. Kim, E. M. Vogel, J. Kim and R. M. Wallace, Appl. Phys. Lett. **93** (25), 252905 (2008).

48. M. Lachab, M. Sultana, H. Fatima, V. Adivarahan, Q. Fareed and M. Khan, Semicond. Sci. Technol. **27** (12), 125001 (2012).

49. R. Vetury, N. Q. Zhang, S. Keller and U. K. Mishra, Electron Devices, IEEE Transactions on **48** (3), 560-566 (2001).

50. M. Fagerlind, F. Allerstam, E. O. Sveinbjornsson, N. Rorsman, A. Kakanakova-Georgieva, A. Lundskog, U. Forsberg and E. Janzen, J. Appl. Phys. **108** (1), 014508 (2010).

51. N. Ramanan, B. Lee, C. Kirkpatrick, R. Suri and V. Misra, Semicond. Sci. Technol. **28** (7), 074004 (2013).

52. D. A. Deen, D. F. Storm, R. Bass, D. J. Meyer, D. S. Katzer, S. C. Binari, J. W. Lacis and T. Gougousi, Appl. Phys. Lett. **98** (2), 023506 (2011).

53. D. A. Deen, D. F. Storm, R. Bass, D. J. Meyer, D. S. Katzer, S. C. Binari, J. W. Lacis and T. Gougousi, Appl. Phys. Lett. **98**, 023506.

54. P. D. Ye, B. Yang, K. K. Ng, J. Bude, G. D. Wilk, S. Halder and J. C. M. Hwang, Appl. Phys. Lett. **86** (6), 063501 (2005).

55. T. Hashizume, S. Ootomo and H. Hasegawa, Appl. Phys. Lett. **83** (14), 2952-2954 (2003).

56. T. Hashizume, S. Ootomo, T. Inagaki and H. Hasegawa, 2003 (unpublished).

57. M. Esposto, S. Krishnamoorthy, D. N. Nath, S. Bajaj, T.-H. Hung and S. Rajan, Appl. Phys. Lett. **99** (13), 133503 (2011).

58. A. D. Carter, W. J. Mitchell, B. J. Thibeault, J. J. Law and M. J. Rodwell, Applied physics express **4** (9), 091102-091102 (2011).

59. E. R. Cleveland, L. B. Ruppalt, B. R. Bennett and S. Prokes, Appl. Surf. Sci. (2013).

60. L. B. Ruppalt, E. R. Cleveland, J. G. Champlain, S. M. Prokes, J. Brad Boos, D. Park and B. R. Bennett, Appl. Phys. Lett. **101** (23), 231601-231601-231605 (2012).

61. G. Kresse and J. Furthmüller, Computational Materials Science **6** (1), 15-50 (1996).

62. G. Kresse and J. Furthmüller, Phys. Rev. B **54** (16), 11169 (1996).

63. G. Kresse and D. Joubert, Phys. Rev. B **59** (3), 1758 (1999).

64. J. P. Perdew, K. Burke and M. Ernzerhof, Phys. Rev. Lett. **77** (18), 3865 (1996).

65. P. E. Blöchl, Phys. Rev. B **50** (24), 17953 (1994).

66. E. A. Chagarov and A. C. Kummel, J. Chem. Phys. **135** (24), 244705-244705-244717 (2011).

67. J. Heyd and G. E. Scuseria, J. Chem. Phys. **121** (3), 1187-1192 (2004).

68. J. Heyd, G. E. Scuseria and M. Ernzerhof, J. Chem. Phys. **118** (18), 8207-8215 (2003).

69. J. Heyd, G. E. Scuseria and M. Ernzerhof, J. Chem. Phys. **124** (21), - (2006).

70. M. Yokoyama, N. Taoka, R. Suzuki, O. Ichikawa, H. Yamada, N. Fukuhara, M. Hata, M. Sugiyama, Y. Nakano, M. Takenaka and S. Takagi, presented at the Indium Phosphide and Related Materials (IPRM), 2012 International Conference on, 2012 (unpublished).

71. N. Goel, P. Majhi, C. O. Chui, W. Tsai, D. Choi and J. S. Harris, Appl. Phys. Lett. **89** (16), 163517 (2006).

72. P. T. Chen, Y. Sun, E. Kim, P. C. McIntyre, W. Tsai, M. Garner, P. Pianetta, Y. Nishi and C. O. Chui, J. Appl. Phys. **103** (3), 034106 (2008).

73. Y. Dong, R. M. Feenstra and J. E. Northrup, 2006 (unpublished).

74. See Supplementary Material Document for more information on modeling the N-polar GaN interface.

75. F. S. Aguirre-Tostado, M. Milojevic, K. J. Choi, H. C. Kim, C. L. Hinkle, E. M. Vogel, J. Kim, T. Yang, Y. Xuan, P. D. Ye and R. M. Wallace, Appl. Phys. Lett. **93** (6), 061907 (2008).

76. H. Sik, Y. Feurprier, C. Cardinaud, G. Turban and A. Scavennec, J. Electrochem. Soc. **144** (6), 2106-2115 (1997).

77. S. Wolter, B. Luther, D. Waltemyer, C. Onneby, S. Mohney and R. Molnar, Appl. Phys. Lett. **70** (16), 2156-2158 (1997).

78. C. Surdu-Bob, S. Saied and J. Sullivan, Appl. Surf. Sci. **183** (1), 126-136 (2001).

79. S. Gu, A. J. Kerr, E. Chagarov, A. C. Kummel and P. M. Asbeck, presented at the 60th AVS Annual Meeting, Long Beach, CA, 2013 (unpublished).